INORGANIC SUBSTRATES AND ENCAPSULATION LAYERS FOR TRANSIENT ELECTRONICS

John Rogers

University of Illinois Champaign

JULY 2014
Final Report

STINFO COPY

AIR FORCE RESEARCH LABORATORY
SENSORS DIRECTORATE
WRIGHT-PATTERSON AIR FORCE BASE, OH 45433-7320
AIR FORCE MATERIEL COMMAND
UNITED STATES AIR FORCE

REPORT DOCUMENTATION PAGE			Form Approved OMB No. 0704-0188

The public reporting burden for this collection of information is estimated to average 1 hour per response, including the time for reviewing instructions, searching existing data sources, searching existing data sources, gathering and maintaining the data needed, and completing and reviewing the collection of information. Send comments regarding this burden estimate or any other aspect of this collection of information, including suggestions for reducing this burden, to Department of Defense, Washington Headquarters Services, Directorate for Information Operations and Reports (0704-0188), 1215 Jefferson Davis Highway, Suite 1204, Arlington, VA 22202-4302. Respondents should be aware that notwithstanding any other provision of law, no person shall be subject to any penalty for failing to comply with a collection of information if it does not display a currently valid OMB control number. **PLEASE DO NOT RETURN YOUR FORM TO THE ABOVE ADDRESS**.

1. REPORT DATE *(DD-MM-YY)* July 2014	2. REPORT TYPE Final	3. DATES COVERED *(From - To)* 9 July 2013 – 25 March 2014

4. TITLE AND SUBTITLE INORGANIC SUBSTRATES AND ENCAPSULATION LAYERS FOR TRANSIENT ELECTRONICS	5a. CONTRACT NUMBER FA8650-13-C-7348
	5b. GRANT NUMBER
	5c. PROGRAM ELEMENT NUMBER 61101E
6. AUTHOR(S) John Rogers	5d. PROJECT NUMBER 1000
	5e. TASK NUMBER N/A
	5f. WORK UNIT NUMBER Y0ZB

7. PERFORMING ORGANIZATION NAME(S) AND ADDRESS(ES) University of Illinois Champaign 1304 W. Green Street Urbana, IL 61801	8. PERFORMING ORGANIZATION REPORT NUMBER AFRL-RY-WP-TR-2014-0140

9. SPONSORING/MONITORING AGENCY NAME(S) AND ADDRESS(ES) Air Force Research Laboratory Sensors Directorate Wright-Patterson Air Force Base, OH 45433-7320 Air Force Materiel Command United States Air Force	10. SPONSORING/MONITORING AGENCY ACRONYM(S) AFRL/RYDD
	11. SPONSORING/MONITORING AGENCY REPORT NUMBER(S) AFRL-RY-WP-TR-2014-0045

12. DISTRIBUTION/AVAILABILITY STATEMENT
Approved for public release; distribution unlimited.

13. SUPPLEMENTARY NOTES
This report is the result of contracted fundamental research deemed exempt from public affairs security and policy review in accordance with SAF/AQR memorandum dated 10 Dec 08 and AFRL/CA policy clarification memorandum dated 16 Jan 09. Report contains color

14. ABSTRACT
The objective of this work was to establish a database of dissolution rates for various inorganic materials relevant to encapsulation layers and substrates for transient electronic systems, and to establish demonstration vehicles for the use of these materials in electronic devices with practical ranges of transient time. The scope of the work was to study the kinetics of dissolution in various solutions, to design and demonstrate an inorganic-based substrate system and encapsulation strategy, and to demonstrate functionality by the integration of simple transient electronic components onto these substrates with encapsulation

15. SUBJECT TERMS
inorganic substrates, transient electronics

16. SECURITY CLASSIFICATION OF:			17. LIMITATION OF ABSTRACT: SAR	18. NUMBER OF PAGES 50	19a. NAME OF RESPONSIBLE PERSON (Monitor) Carrie Bartsch
a. REPORT Unclassified	b. ABSTRACT Unclassified	c. THIS PAGE Unclassified			19b. TELEPHONE NUMBER (Include Area Code) N/A

Standard Form 298 (Rev. 8-98)
Prescribed by ANSI Std. Z39-18

Table of Contents

List of Figures

List of Tables

Table **Page**

1.0   Abstract

The objective of this work was to establish a database of dissolution rates for various inorganic materials relevant to encapsulation layers and substrates for transient electronic systems, and to establish demonstration vehicles for the use of these materials in electronic devices with practical ranges of transient time. The scope of the work was to study the kinetics of dissolution in various solutions, to design and demonstrate an inorganic-based substrate system and encapsulation strategy, and to demonstrate functionality by the integration of simple transient electronic components onto these substrates with encapsulation. This effort reports the hydrolysis kinetics of various biodegradable metals (magnesium, iron, tungsten, molybdenum, zinc) as well as dissoluble dielectrics (silicon oxides, silicon nitrides, spin-on glass). The biodegradable metals are proposed for transient inorganic substrates capable of on-substrate photolithography and resistance to swelling after passivation with silicon oxides and nitrides. The performance of various devices including transistors, diodes, capacitors, and inductors was demonstrated on various metal foil substrates. The strategy of multiple layers of silicon oxides and nitrides significantly reduced water leakage with fully transient encapsulation. The fully integrated system, containing a metal foil substrate and inorganic encapsulation, and transient behaviors were demonstrated.

2.0   Summary

This effort reports the dissolution kinetics of dielectric materials (silicon oxides, nitrides, and spin-on glass), biodegradable metals (magnesium, iron, tungsten, molybdenum, zinc) in various buffer solutions with different pH values, and biofluids. The pH and ion-concentration-dependent dissolution were observed in silicon oxides and nitrides where higher pH and additional cation concentrations (K^+, Na^+, Ca^{2+} and Mg^{2+}) in the solution accelerates hydrolysis. The dissolution rates of silicon oxides and nitrides differed depending on such film properties as film density and stoichiometry, which varied with forming methods (thermally oxidized, chemical vapor deposition and physical vapor deposition). Hydrolysis of spin-on glass was observed and the curing-temperature-dependent dissolution rates were analyzed from knowledge of the concentration of hydroxide bonds (-OH) in the molecules. The consistent dissolution rates of Fe, W, Mo, and Zn metals were observed in two different forms – thin foils and thin-film electrodes.

The performance of encapsulation layers of silicon oxides and nitrides as barriers to water leakage was demonstrated with the resistance stability of Mg electrodes encapsulated with different combinations of oxide and nitride layers. The multiple layers of combined silicon oxides and nitrides enhance stable device performance in aqueous solutions by reducing the possibility of defects in the layers. Atomic layer deposition is a proposed alternative method to the plasma-enhanced chemical vapor deposition method with significantly fewer layer defects.

The thin metal foils were demonstrated as transient inorganic substrates after passivation with silicon oxides, nitrides, and spin-on glass. Transfer printing was possible on passivated metal foil substrates with spin-on glass. On-substrate photolithography, including plasma-enhanced vapor deposition, wet/dry etch, and electron beam evaporation, was compatible with metal foil substrates. Transistors, diodes, and capacitors were successfully fabricated on the metal foil substrates with performance comparable to those on non-degradable substrates. The inductor performed through the high-frequency range (~25 GHz), but had a different inductance characteristic from the on-glass device, an issue that must be considered for future designs. Integrated devices consisting of degradable inorganic materials were demonstrated with metal foil substrates, monocrystalline silicon nanomembrane semiconductors, silicon oxide dielectrics, magnesium electrodes and magnesium oxide encapsulation. Stable device operation was observed while the encapsulation layer was protecting the system, and transient electrical performance followed with the beginning of electrode dissolution.

3.0   Introduction

Biodegradable organic polymers and inorganic metals have important roles in biomedicine, where they serve as passive implants and drug-delivery vehicles that dissolve in the body in a controlled fashion. Although the chemical diversity and easy processing of polymers are advantages in many instances, metals offer superior mechanical properties and additionally do not swell in biofluids. These features of metals are important for applications in biodegradable coronary stents [1] and bone fixation screws/pins [2, 3]. Here, we illustrate that these same characteristics make thin metal foils well suited for use as substrates and encapsulating packages in emerging classes of biodegradable semiconductor devices. Such technology has the potential to dramatically expand the range of functions possible in temporary biomedical devices.

Organic polymers serve as substrates and encapsulating materials, with demonstrated options that range from films of silk fibroin, polycaprolactone (PCL), polyglycolic acid (PGA), polylactic acid (PLA), polylactic-co-glycolic acid (PLGA, a copolymer of PLA and PGA), collagen and even rice paper [4-12]. This set of materials allows fabrication of nearly all types of active and passive electronic components, including resistors, inductors, capacitors, antennas, transistors and diodes [5, 11, 12]. Solar cells, mechanical energy harvesters, strain and temperature sensors, photodetectors and other devices are also possible [5, 6]. Simple system examples include radio frequency (RF) scavenger circuits, complementary metal–oxide–semiconductor (CMOS) ring oscillators and digital imagers for wireless power, RF communication systems and cameras [12]. Although degradable polymer substrates can be useful, their incompatibility with many aspects of semiconductor processing, their tendency to swell and crack the electronic materials they support when immersed in water or biofluids, their poor thermal stability and their non-zero water permeability can limit engineering options in function, durability and processing/manufacturing schemes. By contrast, metal foils are robust, they can provide hermetic protection, they are compatible with most device fabrication steps, and they are thermally and chemically stable. The results presented below illustrate the utility of molybdenum, iron, tungsten and zinc foils as platforms for water-soluble electronics and of silicon oxides, silicon nitrides and spin-on glass materials as passivating and bonding interlayers for these foils.

Dissoluble insulation, passivation and encapsulation in biodegradable microelectronics are critically important for proper device operation. Silicon oxides and nitrides are in widespread use not only for digital and analog circuits but also for thin-film display electronics and others, due to their excellent properties as gate and interlayer dielectrics, passivation coatings, and barriers against water penetration. Here we suggest using silicon oxides and nitrides as inorganic dissoluble encapsulants by examining the water permeability and hydroylysis kinetics in various aqueous solutions. The integrated system with metal foil substrate and inorganic encapsulation demonstrates a fully degradable transient electronic system.

4.0   Methods, Assumptions, and Procedures

4.1   Dissolution Studies of Silicon Oxides, Nitrides and Spin-on Glass

4.1.1   Test structures for Silicon Oxides and Nitrides

Thin layers of silicon oxides (SiO_2) were prepared in three different ways, all on silicon wafers (University Wafer):
(1) Thermally grown (tg-oxides) (dry and wet oxidation)
(2) Plasma-enhanced chemical vapor deposition (PECVD) from precursor gases (Trion Technology, USA) at 350 ℃
(3) Electron beam (E-beam) evaporated from SiO_2 pellets (99.99%, Kurt J. Lesker Company, USA)

The nitrides were deposited onto similar wafers. The films were formed by low-pressure chemical vapor deposition (LPCVD) and by PECVD (Surface Technology Systems, Newport, UK) at 300 ℃ using low frequency (LF, 380 kHz) and high frequency (HF, 13.56 MHz). In all cases, the thickness was controlled at ~100 nm. The test structures for atomic force microscopy measurement consisted of arrays of square pads (3 μm × 3 μm × 100 nm) of PECVD and E-beam oxides on tg-oxide on Si wafer, fabricated by photolithography and reactive ion etching (RIE).

4.1.2   Dissolution Experiments

Samples were placed into 50 mL of aqueous buffer solutions with different pH values (pH 7.4−12, Sigma-Aldrich, USA) at either room temperature (RT) or physiological temperature (37 °C). Studies also involved bovine serum (pH ~7.4, Sigma-Aldrich, USA) at 37 °C and sea water (pH ~7.8) at room temperature. In all cases, the samples were removed from the solutions, rinsed with deionized (DI) water, and measured by spectroscopic ellipsometry (J. A. Wooldman Co. Inc., USA) to determine thickness and/or atomic force microscopy (AFM) (Asylum Research MFP-3D, USA) to determine both the thickness and surface morphology. After such measurements, each of which lasted a few hours, the samples were returned to the solutions. The solutions were replaced every other day.

4.1.3   Characterization of Film Properties

Film density was measured using an x-ray reflectometry (XRR) (X'pert MRD System, Netherlands) and x-ray photoelectron spectroscopy with a system from Axis ULTRA, UK. To avoid surface oxidation of the nitrides, the measurements were conducted shortly after oxide removal in buffered oxide etchant (BOE) 6:1 (Transene Company Inc., USA) for a few seconds. Transmission electron microscopy (TEM) (JEOL 2010F (S)TEM, USA) was used to study the porous microstructure of the PECVD and E-beam oxides.

4.1.4 Dissolution Tests of Spin-on Glass

Silicate-based spin-on glass (cast on Si wafer and cured at 300 °C, 400 °C and 800 °C for 1 hour), each sample was placed into 50 ml of phosphate buffer solution (PBS) pH 7.4 (Sigma-Aldrich, USA) at 37 °C. The samples were removed from the solution, rinsed with DI water, and the thicknesses were measured by profilometer (Dektak 3030, Sloan Technology Co., USA) for metal foils and spectroscopic ellipsometry (J. A. Wooldman Co. Inc., USA) for spin-on glass (SOG). The hydroxide functional groups for SOG was investigated by Fourier-transform infrared spectroscopy (FTIR) (Thermo Nicolet Nexus 670, USA) in diffuse reflection mode. After measurement, the samples were re-immersed in fresh solutions. The solutions were replaced every other day.

4.2 Hydrolysis Kinetics of Biodegradable Metals

4.2.1 Test Structures and Deposition Method

Patterned, serpentine traces of thin metal films (40 nm-300 nm) deposited by electron beam evaporation (Fe) (AJA Orion 3 sputter system, N. Scituate, MA) or by magnetron sputtering (all others) (AJA Orion 8 evaporation system, N. Scituate, MA) were patterned by photolithography (AZ® nLOF™ 2070 photoresist) and lift-off on glass substrates. The deposition conditions were 0.1 nm/s for Fe; 50 W, 3 mT for Mg and AZ31B Mg alloy; 100 W, 100 mT for Zn; 150 W, 5 mT for W; 150 W, 3 mT for Mo. These conditions minimize delamination and maintain high quality, uniform films with good yield. A layer of Cr (10 nm) deposited by either sputtering or electron beam evaporation served as an adhesion promoter, to eliminate delamination during the dissolution tests. The chemical vapor deposition (CVD) W (150nm) samples were provided by MIT Lincoln Laboratory. Grain size of the deposited thin films was evaluated from x-ray diffraction (XRD) data analyzed with Jade software: Fe (10nm); Mg (22 nm); AZ31B (24 nm); Zn (13 nm); sputtered W (16 nm); CVD W (55 nm); and Mo (30 nm).

4.2.2 Dissolution Experimental

Dissolution behavior was studied in naturally aerated DI water and Hanks' solution (H 8264, Sigma-Aldrich®, St. Louis, MO). As a control experiment with Mo (40 nm thick, in Hanks' solution at pH 8, for 250 h), air was continuously bubbled through the solution. The dissolution rate was found to be similar to those without bubbling. Given the known sensitivity of Mo dissolution to O_2 concentration, this result suggests that the O_2 concentration in the solutions is in equilibrium with air and does not vary significantly over time. Small amounts of NaOH and HCl were added to the Hanks' solutions to control the pH. A Hanna HI 9126 portable pH/ORP meter (HANNA instruments, Smithfield, RI) was used to monitor the pH at various times during dissolution, to ensure that the value remained constant during the experiment (±0.2 pH units). Furnace with constant temperature of 37 °C was used to conduct dissolution at body temperature. Electrical probing occurred through contacts to two pads located outside of the solution. The thicknesses of patterned metal thin films in DI water were also monitored, even after complete loss of electrical continuity, with solutions replaced every other day to avoid reaching the solubility limits.

4.2.3 Fabrication of Transistor for Measurement of Electrical Transience with Different Metal Electrodes

N-channel metal–oxide–semiconductor field-effect transistors (MOSFETs) were prepared on silicon-on-insulator (SOI) wafers (320 nm top silicon layer, p-type, SOITEC, France). The source and drain areas were doped through diffusion of phosphorous at ~1000 ^{o}C for 5 minutes with thermal oxides as the doping mask, to yield a concentration of ~10^{20} cm^{-3}. The top device silicon was patterned by RIE with sulfur hexafluoride (SF$_6$) gas. The gate dielectrics (SiO$_2$, ~130 nm) were formed by PECVD at 250 ^{o}C, and patterned by photolithography and etching in BOE. Metal contacts were deposited using the same methods as mentioned previously, but without the Cr adhesion layer. The transient electrical properties of the MOSFETs were evaluated using a probe station and semiconductor parameter analyzer (Agilent 4155C, Agilent Technologies, Santa Clara, CA).

4.2.4 Characterization Method for Hydrolysis Kinetics of Metals

A Hitachi S-4800 high resolution scanning electron microscope (SEM) (Hitachi high-technologies corporation, Japan) was used to examine the surface and cross-sectional morphologies of metal films at various stages of dissolution in DI water, using 10 kV applied voltage and 4 mm working distance. The surface chemistry was determined by using x-ray photoelectron spectroscopy (XPS). High-resolution XPS measurements were made with a Kratos Axis Ultra photoelectron spectrometer (Kratos Analytical, Inc., Manchester, UK) using monochromatic Al Ka radiation (1486.6 eV) at a pass energy of 40 eV. The binding energy scale was referenced to the adventitious C 1s signal at 285 eV (except for Mg and Mg alloys which were referenced to 286 eV). The dissolution products and film morphologies were also studied by JEOL 2010LaB$_6$ TEM (JEOL USA, Inc., Peabody, MA), with an applied voltage of 200 kV and camera constant of 13.4 mm. TEM samples were prepared by depositing 100 nm of Mg and AZ31B Mg alloy, and 50 nm of Zn, W, Mo and Fe on 15 nm silicon nitride grids (Ted Pella, Inc., Redding, CA). These samples were immersed in DI water for 0.5 hours (Mg), 1 hour (AZ31B Mg alloy), 10 hours (W), 40 hours (Mo), 2 hours (Zn) and 2 days (Fe) before TEM analysis. A surface profilometer (Veeco/Sloan Dektak 3 ST, Plainview, New York) was used to determine the changes in thicknesses of metal thin films at various stages of dissolution in DI water. Reported thickness data corresponds to average thicknesses evaluated at ten different locations. The standard deviations of the data was used as the error bars.

4.3 Fabrication of Integrated Inorganic Substrate and Encapsulants

4.3.1 Fabrication of Transient Electronics (N-channel Silicon Transistor, Si PIN Diodes, Capacitors and Inductors) on Dissolvable Metal Substrates

Fabrication began with laminating iron (Fe), molybdenum (Mo), tungsten (W) and zinc (Zn) foils (~10 μm thick; Goodfellow, USA) on poly(dimethylsiloxane) (PDMS) (Dow Corning, USA) coated on glass slides to facilitate processing. SiO$_2$ (~1 μm) was deposited by PECVD on these foils for electrical isolation. Functional silicon (Si) nanomembranes (NM) were created from SOI wafers (SOITEC, France) by solid-state phosphorus doping at 950 °C and boron doping at 1000 °C to define active regions for transistors and diodes. After removal of the

buried oxide by hydrofluoric acid (HF), the Si NMs were transfer-printed onto a thin layer of silicate SOG (Filmtronics Inc., USA) cast on the SiO_2 coated foils, followed by curing at 250 °C for 1 hour. The top device layer was patterned by RIE (Plasmatherm) with SF_6 gas through a photo-patterned resist S1805 (Microchem, USA). For the n-channel MOSFET, PECVD SiO_2 (~100 nm) was used as a gate dielectric, and openings for source and drain contacts were defined by etching with 6:1 BOE (Transene Company Inc., USA). Patterned Mg (~300 nm) electrodes were defined by a lift-off process with photoresist AZ2070 (Microchem, USA), and E-beam evaporation to complete the fabrication. The bottom electrodes for both capacitors and inductors were defined with Mg (~300 nm) by lift-off. A layer of PECVD SiO_2 (~900 nm) was used for the interlayer dielectrics. A thick layer of Mg (~3.5 μm) formed the top contacts. The completed devices were released from PDMS after immersion in pentane for ~2 hours.

4.3.2 Study of Functional Transience at the Device Level after Encapsulated

Transient active and passive components were fabricated on Mo foils (~10 μm) as described in previous sections. MgO (~1 μm for transistors and diodes and ~3 μm for capacitors and inductors) was deposited to encapsulate the transient devices, except at contact pads for probing electrical properties. The devices were partially immersed into DI water at room temperature during measurements of electrical function.

5.0   Results and Discussion

5.1   Study of Kinetics of Dissolution

5.1.1   Contractor will Measure Key Performance Characteristics of CVD-based Silica or Spin-on-glass Layers for Encapsulation of Transient Electronics

5.1.1.1 Characterization of Performance of PE-CVD SiO$_2$ and SiN$_x$ as Encapsulants

We proved that defects, such as pinholes, are a primary cause for leakage of vapors or fluids from the previous studies of encapsulation with PECVD oxide and nitride in organic light-emitting diode (OLED) studies. As shown in Figure 1a (left), a combination of multiple different layers, i.e. SiO$_2$ and Si$_3$N$_4$, improves the performance by acting as an encapsulation. Multiple layers with different materials can reduce water/vapor permeation through an underlying layer, by cooperative elimination of defects. In addition to PECVD based multiple layers, atomic layer deposition (ALD) provides a complementary strategy to reduce effects arising from defects. A double layer of PECVD SiO$_2$ (or PECVD Si$_3$N$_4$) and ALD SiO$_2$ provides effective means of encapsulation, even with thin layers (Figure 1a, right).

Figure 1b presents measured changes in resistance of a serpentine-shaped Mg trace (~300 nm), with several encapsulation approaches at various times for immersion in deionized water at room temperature. If the resistance is stable while immersing in water, the encapsulation prevents the penetration of water molecules. We checked the time of this stable period to compare the performance of encapsulation. Samples with a single layer of ALD SiO$_2$ (~20 nm), PECVD SiO$_2$ or Si$_3$N$_4$ (~1 μm) show an increase in resistance after just a few hours of immersion. A combination of PECVD SiO$_2$ (~500 nm) and Si$_3$N$_4$ (~500 nm) extends this time to ~1 day. Triple layers of PECVD SiO$_2$ and Si$_3$N$_4$ (~200 nm/ 200 nm/ 200 nm/ 200 nm/ 100 nm/ 100 nm, total thickness ~1 μm) extend to ~10 days. Combinations of PECVD SiO$_2$/ALD SiO$_2$ (~500/20 nm) and PECVD Si$_3$N$_4$/ALD SiO$_2$ (~500/20 nm) show characteristic times of ~5 and ~7 days, respectively. These results suggest that the ALD SiO$_2$ layer has significantly fewer defects than PECVD SiO$_2$ or Si$_3$N$_4$. A single layer of ALD (~20 nm) provides a similar timescale as a single layer of SiO$_2$ or Si$_3$N$_4$ (~1 μm).
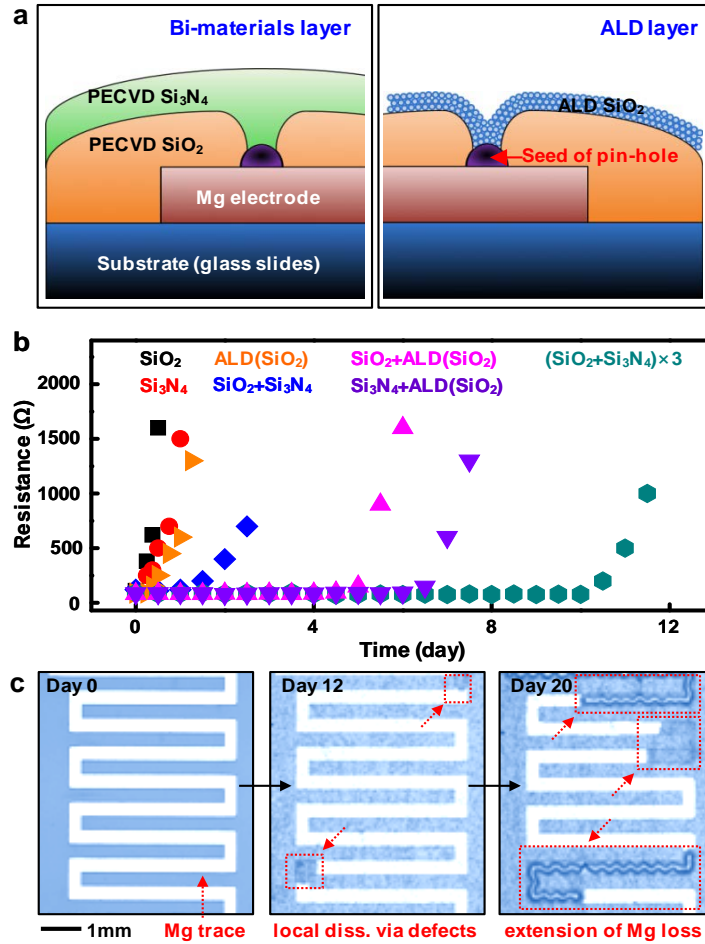
Figure 1: Encapsulation Approaches with Transient Materials

a) Schematic illustrations of encapsulation methods for transient electronic devices, showing defects (e.g. pinholes) covered by a bilayer of SiO_2/Si_3N_4 (left); ALD provides a defect-free layer (right). b) Measurements of changes in resistance of Mg traces (~300 nm thick) encapsulated with different materials and thicknesses while immersed in deionized (DI) water at room temperature. A single layer of ALD SiO_2 (orange, 20 nm), PECVD SiO_2 (black, 1 μm) and PECVD low frequency (LF) Si_3N_4 (red, 1 μm), a double layer of PECVD SiO_2/PECVD-LF Si_3N_4 (blue, 500/500 nm), PECVD SiO_2/ALD SiO_2 (magenta, 500/20 nm), PECVD-LF Si_3N_4/ALD SiO_2 (purple, 500/20 nm), and a triple layer of PECVD SiO2/PE-CVD-LF Si_3N_4 (Cyan, 200/200/200/200/100/100 nm) were used for the encapsulation. c) A series of micrographs of a serpentine trace of Mg (initially ~300 nm thick) while dissolution in DI water at room temperature. Dissolution begins from local defects and then rapidly propagates outward.

We observed two-stage kinetics in the functional transience of this test structure: i) encapsulation layers define the first time period, i.e. stable operation with negligible changes in electrical properties, ii) the Mg defines the second, i.e. rapid degradation in function. The optical microscope images in Figure 1c clearly reveal that the dissolution of Mg begins with the leakage of water from local defects, which then quickly propagate laterally. These results suggest that an

9

efficient encapsulation strategy is critically important in removing these leakage pathways to increase the time of stable operation.

5.1.1.2 Evaluation of Hydrolysis Mechanism of SOG Layers

We evaluated the kinetics of hydrolysis of SOG with different curing temperatures and time, after immersion in PBS (pH 7.4) at 37 °C in Figure 2a. Material cured at 300 °C dissolves faster (~50 nm/day) than that cured at 800 °C (~6 nm/day). The 4 hours cured SOG dissolved slower than SOG cured for 1 hour. In Figure 2b, we used FTIR to reveal the dependence of OH content on curing temperatures. Figure 2b shows the spectra of the SOG prepared at three different curing temperatures. The stretching modes between 3600 and 3200 cm^{-1}, which reflect the -OH content, shows that the SOG cured at 300 °C has more –OH compared to that at 800 °C. The curing involves a high-temperature condensation reaction of $Si(OH)_4$, and associated shrinkage as described in Figure 2c. The extent of this reaction varies depending on the curing temperature and time; the non-reacting parts remain as Si-OH. Consequently, SOG cured at lower temperature, has higher Si-OH content, and faster rates of hydrolysis. This result provides tunability of the dissolution rate through control of the curing temperature and time.
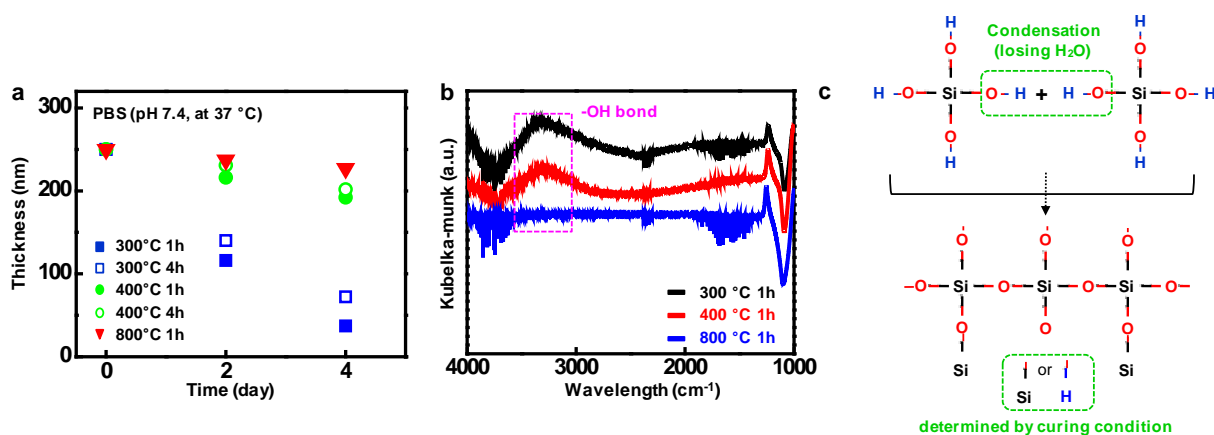
Figure 2: Dissolution Kinetics of Spin-on Glass
a) Measured dissolution rates of SOG cured at different temperatures in PBS, pH 7.4 at physiological temperature (37 °C) (black, 300 °C; red, 400 °C; blue, 800 °C; cured for 1 hour). b) Chemical structure of SOG cured at various temperatures, observed by FTIR spectroscopy (black, 300 °C; red, 400 °C; blue, 800 °C; cured for 1 hour). The concentration of the hydroxide groups decreases as the curing temperature increases. c) Chemistry associated with the curing process.

5.1.2   Contractor will Identify Key Control Parameters for Tuning the Water Permeability, Dissolution Kinetics, and Dimensional Change Due to Swelling in Addition to Critical Electromagnetic Properties that Could Affect Subsequent Electronic/RF Circuits Integrated with the Packaging Layers under Study (e.g. Complex Dielectric Constant)

5.1.2.1 Dissolution Kinetics of Various Classes of Silicon Oxides

We examine materials in forms and with chemistries that are widely utilized in the semiconductor industry, as thin films are grown or deposited using standard or slightly modified techniques. The results reveal essential aspects of hydrolysis in such cases, including the influence of morphology and chemistry, as defined by the conditions and methods for deposition. Previous work [13-15] on bulk materials established that the mechanism for hydrolysis of silicon oxides is $SiO_2 + 2H_2O \rightarrow Si(OH)_4$ and the reaction rate depends on OH concentration. To examine the dependence of the dissolution rate on pH and type of oxide, we performed systematic studies in buffer solutions with pH between 7.4 and 12 and at different temperatures. We examined three different classes of materials – thin films of oxides formed by 1) growth using dry (O_2 gas) and wet (H_2O vapor) thermal oxidation (tg-oxide), 2) PECVD oxide, and 3) E-beam oxide evaporation.

We used spectroscopic ellipsometry (J. A. Wooldman Co. Inc., USA) to reveal the dissolution rate as a time dependent change in thickness and AFM (Asylum Research MFP-3D, USA) to provide information on the surface topography as well as independent measurements of thickness. Test structures of PECVD and E-beam materials for AFM measurements consisted of arrays of isolated square films (3 μm × 3 μm × 100 nm) patterned on tg-oxide, whose dissolution rate is much slower than that of other materials, as shown subsequently. Figure 3a presents a schematic illustration of a test structure, and an optical micrograph in the inset. Figures 3b and 3c provide AFM images and thickness profiles at several stages of immersion in an aqueous buffer solution (pH 12) at 37 °C. Figure 4 indicate AFM image and thickness profiles of PECVD oxide in different pH solutions. These results indicate that the oxides dissolve in a uniform fashion, without any significant change in surface topography, formation of flakes or other non-ideal behaviors like those observed, for example, in transient metals under similar conditions.
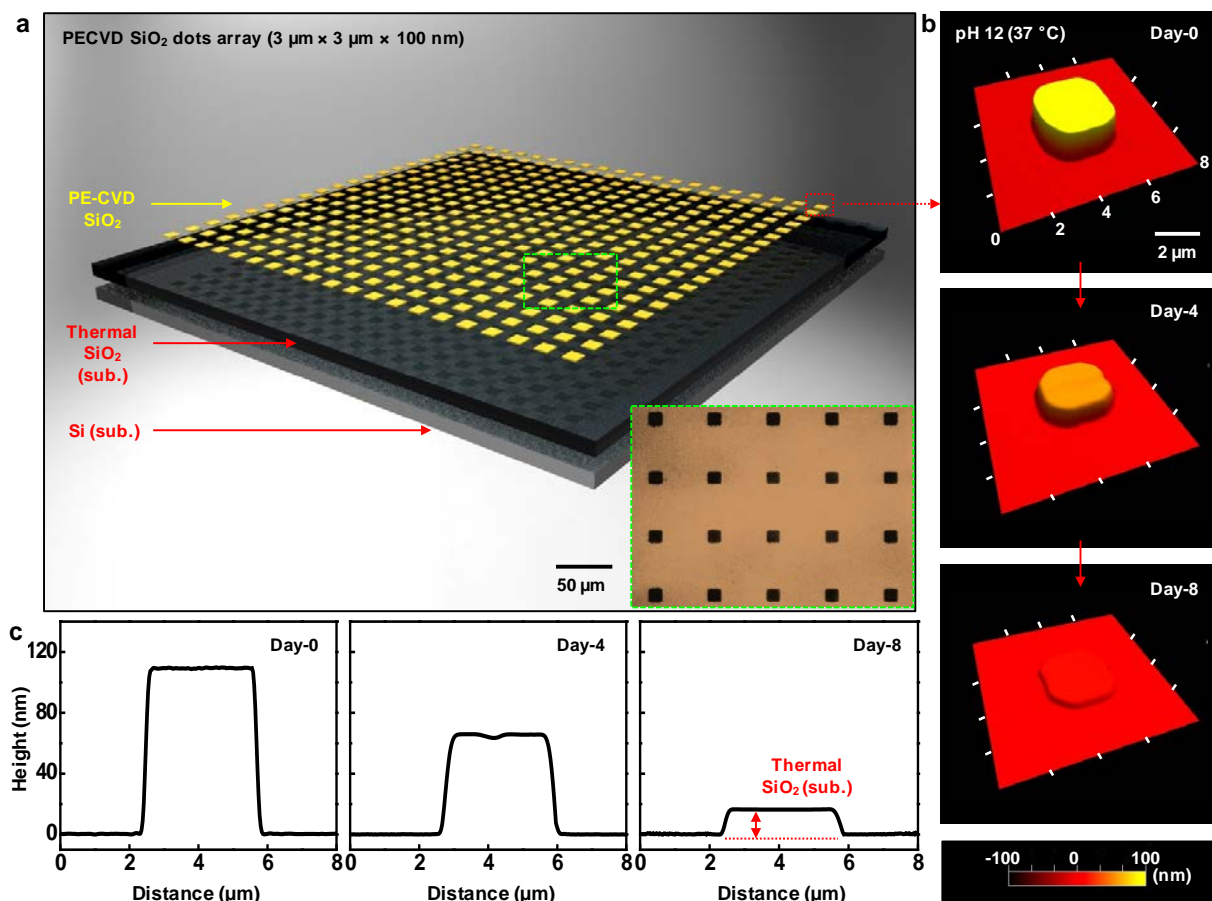
Figure 3: Images and Data from a Structure for Testing the Dissolution of Thin (~100 nm thick) Square Pads of SiO₂ formed by PECVD

a) Schematic illustration of the test structure, which consists of an array of square pads (3 μm × 3 μm × 100 nm) of PECVD SiO₂ deposited at 350 °C on a thermally grown oxide (tg-oxide) on a silicon (100) wafer, with inset optical micrograph. b) AFM topographical images and c) profiles of a representative pad at different stages of hydrolysis in buffer solution (pH 12) at physiological temperature (37 °C).
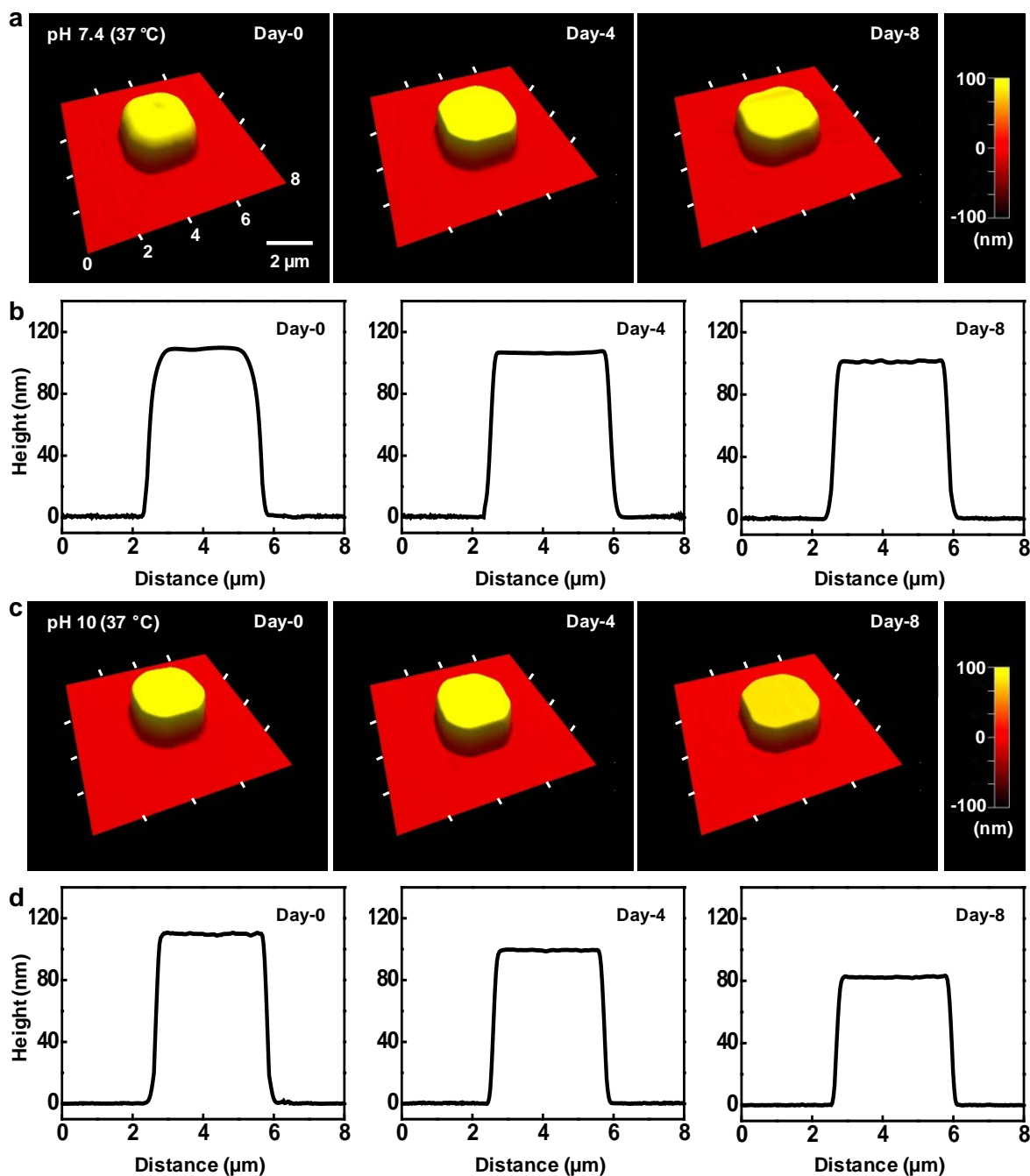
Figure 4: AFM Topographical Images and Profiles of a Representative Pad at Different Stages of Hydrolysis of PECVD

Oxide in buffer solution with pH 7.4 (a,b) and 8 (c,d) at physiological temperature (37 °C)

We investigated the dissolution kinetics of tg-oxide, PECVD oxide and E-beam oxide in terms of the change in thickness as a function of time in buffer solutions (pH 7.4 to 12) at RT and 37 °C in Figure 5a-c. The tg-oxides and E-beam oxide exhibit the slowest and fastest rates, respectively, under the same conditions. Four main factors affect the rate: temperature, pH and ionic content of the solutions, and chemical/morphological properties of the films. The dissolution rate of each oxide increases with temperature, with an expected Arrhenius dependence, consistent with previous studies. We observed a linear dependence of the dissolution rate for each type of oxide in buffer solutions with different pH at 37 °C (Figure 5d). The relationship can be written log $r = a + n$ [pH], where r is the dissolution rate, and a and n are constants ($n=0.33$ for quartz when r is in mol/m^{2}s). The values of n for the data in Figure 5d are between 0.31 to 0.44 (at 37 °C). Figure 5e shows the dependence of the dissolution rate on the film density (~2.3 g/cm^3 for tg-oxides, ~2.1 g/cm^3 for PECVD oxide, ~1.9 g/cm^3 for E-beam oxide). Reduced density can enhance the ability of aqueous solutions to diffuse into the material, thereby accelerating the hydrolysis reaction by increasing the reactive surface area. The kinetics can also be influenced by the concentration of ions in the solution. We performed the dissolution test in bovine serum (pH ~7.4) and sea water (Figure 6) and they show dissolution rates that are ~9 and ~4 times higher than those observed at a similar pH in buffer solution, respectively. This is likely due to the presence of additional ions (ex. K^+, Na^+, Ca^{2+} and Mg^{2+}) in these liquids.
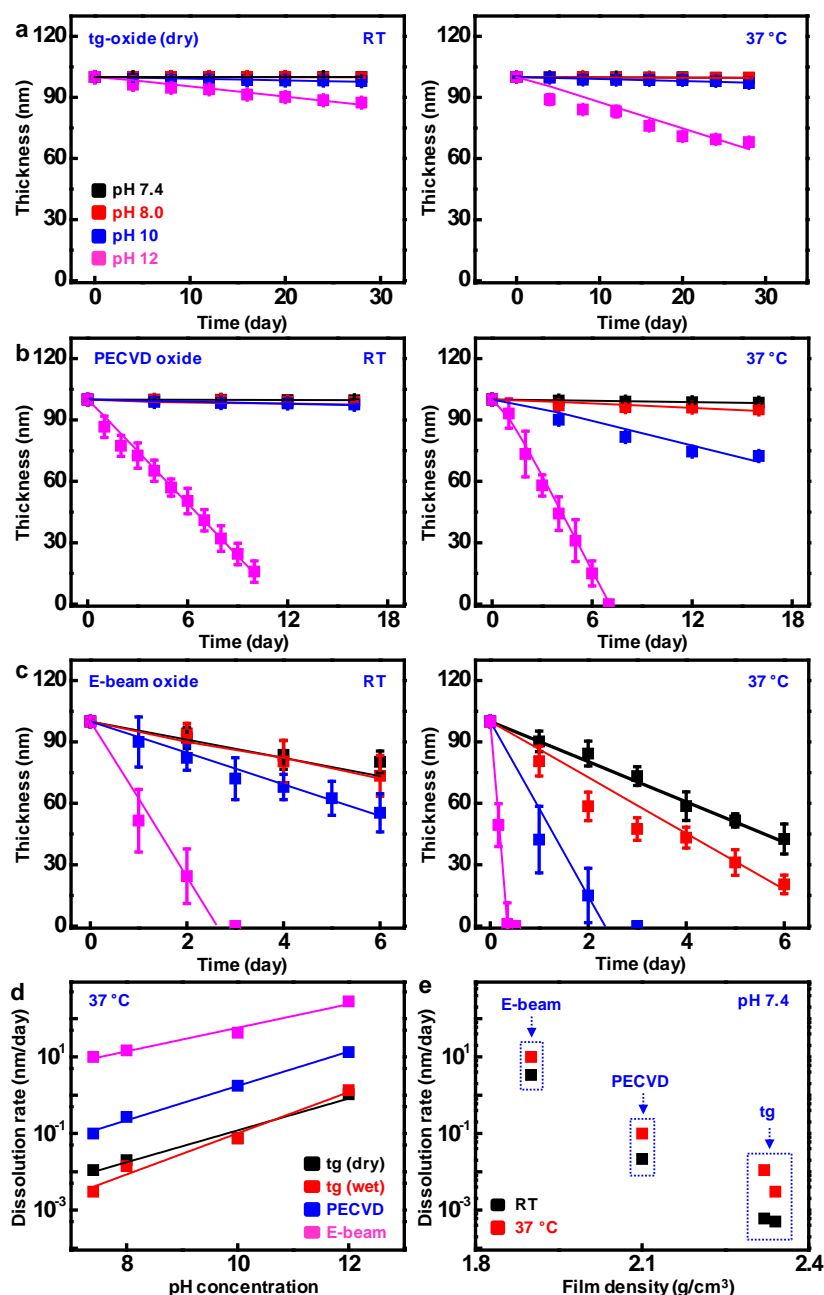
Figure 5: Dissolution Kinetics

As defined by the rate of change of film thicknesses, of different silicon oxides in various aqueous solutions, with different values of pH at room and physiological temperatures. a) Calculated (lines) and measured (symbols) values for the time-dependent dissolution of thermally grown SiO_2 (dry oxidation) in buffer solutions (black, pH 7.4; red, pH 8; blue, pH 10; magenta, pH 12) at room (left) and physiological (right, 37 °C) temperature. b) Calculated (lines) and measured (symbols) dissolution behaviors of PECVD SiO_2 in diverse aqueous solutions with different pH at room (left) and physiological (right, 37 °C) temperature. c) Calculated (lines) and experimental (symbols) results of dissolution studies on E-beam SiO_2 in aqueous solutions at different pH and temperature. d) Dependence of dissolution kinetics of silicon oxide films on pH

15

Figure 6: Dissolution of Various Oxides in the Practical Solutions with Different Ion Concentrations

Thickness changes in a) Bovine serum at body temperature and b) sea water at room temperature

We performed the series of investigations of physical and chemical properties of various classes of oxides to figure out the key properties which affect the dissolution rates. XPS and XRR reveal the stoichiometries, atomic bond configurations and densities. The tg-oxide (dry oxidation) and PECVD oxide have chemistries close to SiO_2 (i.e., Si : O = 1 : 2), while the E-beam oxide is oxygen rich, at $SiO_{2.2}$ (Si : O = 1 : 2.2), as shown in Table 1. The Si 2P spectra (Figure 7a) indicate that the Si-O bond energies are almost identical for the three oxides. Dissolution can occur not just at a molecular level, but also through removal of nanoscale pieces of material that might be released from the film as narrow regions of the porous matrix disappear by hydrolysis. Our careful transmission electron microscopy studies (Figure 7b,c) suggest, however, that the porous structures in the PECVD and E-beam oxides do not involve voids with dimensions larger than one or two nanometers.

Table 1. Atomic Concentration of Different Silicon Oxides Measured by XPS
Carbon (C) and fluorine (F) are considered surface contamination

(%)	Si	O	C	F	x (SiO_x)
tg-SiO₂ (dry)	31.6	64.0	4.3	0.1	2.0
PECVD SiO₂	31.5	63.5	3.6	1.4	2.0
E-beam SiO₂	27.5	61.3	10.8	0.4	2.2
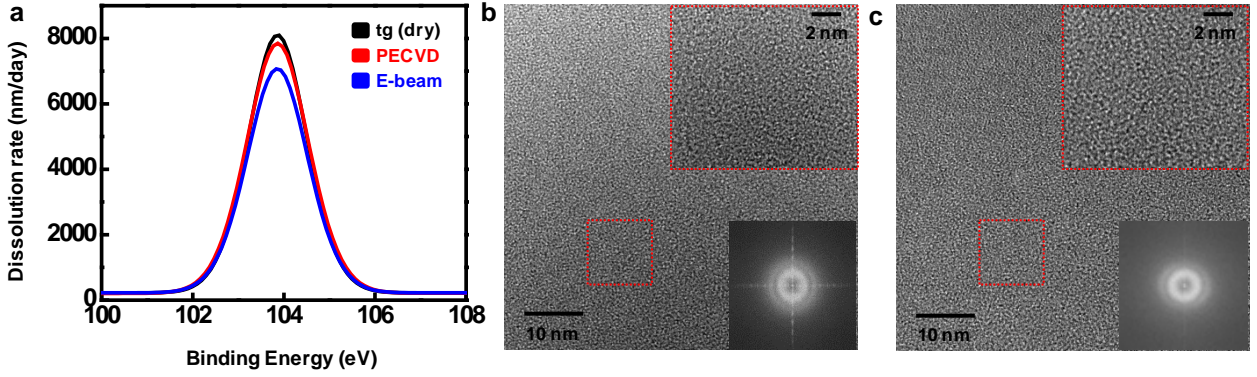
Figure 7: a) Binding Energy between Si and O Bond for Three Different Oxides in this Study Investigated by XPS. The Topography and Diffraction Pattern Observed by TEM for b) PECVD Oxides and c) E-beam Oxides

We proposed the modified reactive diffusion model to capture the effect of diffusion on dissolution rates from the difference of the density of oxides. A modified version of this model, assuming applicability of continuum physics, provides a simple, approximate means to incorporate the effect of density variations associated with porosity. Here, the concentration of water w in the porous material is first determined from the partial differential equation for reactive diffusion $D_e\, \partial^2 w / \partial z^2 - kw = \partial w / \partial t$, where z is the coordinate in the film thickness direction, t is the time, k and De are the reaction constant and the diffusivity in the porous media, respectively. Since the mass of the air pore is negligible compared with that of the porous material, the effective density ρ_{eff} of the porous material is related to the density ρ_s of the fully dense material as

$$\rho_{eff} = \frac{V_s}{V_{air} + V_s}\rho_s \quad ,$$

(1)

where V_s and V_{air} are the volumes of material and air pore, respectively. At time t=0, the air pores are filled with water, or $w|_{t=0} = w_0 \left(\rho_s - \rho_{eff}\right)/\rho_s \ \left(0 \le z < h_0\right)$, where h_0 is initial thickness. The water concentration is constant at the top surface of the material $w|_{z=h_0} = w_0$ ($w_0 = 1$ g/cm^3) and the water flux is zero at the bottom surface $\partial w / \partial z|_{z=0} = 0$. By the method of separation of variables, the water concentration field can be written

$$w(z,t) = w_0 \left\{ \frac{\cosh\left(\sqrt{\frac{kh_0^2}{D_e}}\frac{z}{h_0}\right)}{\cosh\sqrt{\frac{kh_0^2}{D_e}}} + 2\pi\sum_{n=1}^{\infty} B_n (-1)^n \left(n - \frac{1}{2}\right) e^{-\left[\frac{kh_0^2}{D_e} + \left(n - \frac{1}{2}\right)^2 \pi^2\right]\frac{D_e t}{h_0^2}} \cos\left[\left(n - \frac{1}{2}\right)\pi\frac{z}{h_0}\right] \right\} \quad ,$$

(2)

where B_n is

$$B_n = \frac{1}{\frac{kh_0^2}{D_e}+\left(n-\frac{1}{2}\right)^2\pi^2} + \frac{\frac{\rho_{eff}}{\rho_s}-1}{\left(n-\frac{1}{2}\right)^2\pi^2}.$$ (3)

When one mole of material reacts with q moles of water, then integration of materials dissolved at each location through the thickness and over time leads to an expression for the remaining thickness h, normalized by its initial thickness h_0 as

$$\frac{h}{h_0}=1-\frac{w_0 M}{q\rho_{eff}M_{H_2O}}\frac{kh_0^2}{D_e}\left\{\frac{D_e t}{h_0^2}\frac{\tanh\sqrt{\frac{kh_0^2}{D_e}}}{\sqrt{\frac{kh_0^2}{D_e}}}-2\sum_{n=1}^{\infty}B_n\frac{1-e^{-\left[\frac{kh_0^2}{D_e}+\left(n-\frac{1}{2}\right)^2\pi^2\right]\frac{D_e t}{h_0^2}}}{\left[\frac{kh_0^2}{D_e}+\left(n-\frac{1}{2}\right)^2\pi^2\right]}\right\},$$ (4)

where M and M_{H_2O} are the molar masses of porous material and water, respectively. The effective diffusivity of water in a porous medium is linearly proportional to the pores available for the transport, which is equivalent to the air fraction in the porous medium

$$D_e \propto \frac{V_{air}}{V_{air}+V_s}=\frac{\rho_s-\rho_{eff}}{\rho_s}.$$ (5)

The density of SiO_2 is 2.33 g/cm³, 2.10 g/cm³ and 1.90 g/cm³ for the case of thermally grown, PECVD and E-beam oxides, respectively. If SiO_2 with a density of 2.34 g/cm³ has a diffusivity of 8×10^{-16} cm²/s at body temperature, then the diffusivities for PECVD SiO_2 and E-beam SiO_2 can be calculated from Equation (5) as 1.6×10^{-14} cm²/s and 2.92×10^{-14} cm²/s. Reaction constants are fitted to the experimental data and the dissolution rate, $-dh/dt$, is then estimated from

$$-\frac{dh}{dt}=\frac{w_0 M}{q\rho_{eff}M_{H_2O}}kh_0\left\{\frac{\tanh\sqrt{\frac{kh_0^2}{D_e}}}{\sqrt{\frac{kh_0^2}{D_e}}}-2\sum_{n=1}^{\infty}B_n e^{-\left[\frac{kh_0^2}{D_e}+\left(n-\frac{1}{2}\right)^2\pi^2\right]\frac{D_e t}{h_0^2}}\right\},$$ (6)

which can be simplified to

$$-\frac{dh}{dt}=\frac{w_0 M}{q\rho_{eff}M_{H_2O}}kh_0\frac{\tanh\sqrt{\frac{kh_0^2}{D_e}}}{\sqrt{\frac{kh_0^2}{D_e}}}.$$ (7)

In Figure 5a-c, the reaction constants (k) are 1.7×10^{-9} (tg-oxide with dry oxidation), 1.6×10^{-8} (PECVD oxide), and 1.3×10^{-9} (E-beam oxide) s^{-1} in buffer solution with a pH of 7.4 at 37 °C. The results suggest that density influences the dissolution rate not only through changes in rates for diffusion into the material, but also through differences in reactivity.

We investigate the other possibility that dissolution can occur through the removal of nanoscale pieces of material that might be released from the film as narrow regions of the porous matrix disappear by hydrolysis. We performed careful TEM (JEOL 2010F, USA) studies (Figure 7b) and confirmed that the porous structures in the PECVD and E-beam oxides do not involve voids with dimensions larger than one or two nanometers. AFM observation of surfaces with sub-nanometer roughness (average roughness < 0.4 nm, Figure 8) throughout the course of the dissolution process also supports the notion that the film disappears uniformly and gradually, at the molecular level, without the release of pieces of material.
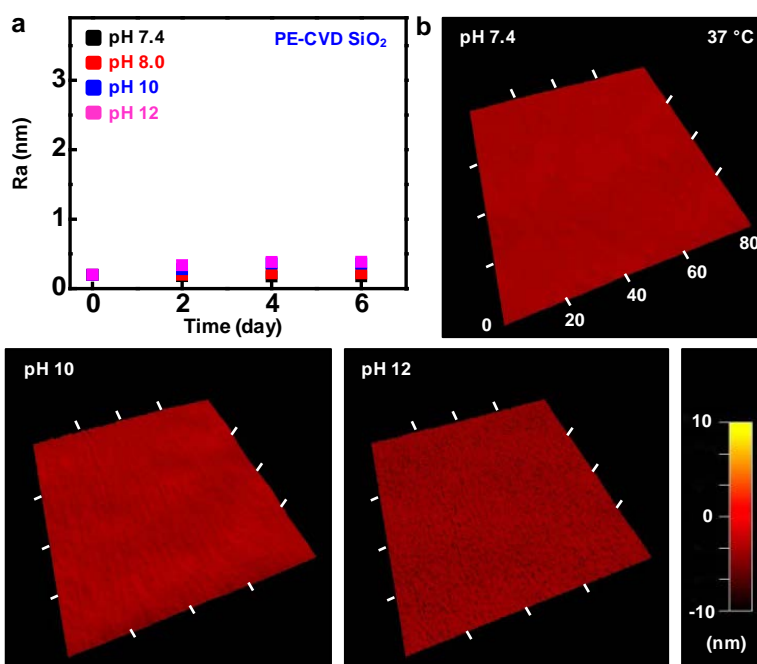
Figure 8: Surface Topography of PECVD after Inmersion into Different Kinds of Buffer Solutions
a)The average roughness of dissolved surface and b) the AFM image 4 days after immersed into the solution.

5.1.2.2 Dissolution Kinetics of Various Classes of Silicon Nitrides

We performed studies of the dissolution kinetics of silicon nitrides in procedures and under conditions similar to those for the silicon oxides. Silicon nitride hydrolyzes in aqueous solution in two steps: (1) oxidation into silicon oxide ($Si_3N_4 + 6H_2O \rightarrow 3SiO_2 + 4NH_3$) and (2) hydrolysis of silicon oxide ($SiO_2 + 2H_2O \rightarrow Si(OH)_4$), where the overall reaction is $Si_3N_4 + 12H_2O \rightarrow 3Si(OH)_4 + 4NH_3$. Because silicon dioxide serves as an intermediate product in these reactions, the dependence of rate on pH might be expected to be similar to that observed in the oxides. We used LPCVD and PECVD techniques to form the silicon nitrides studied here. For PECVD

19

nitrides, two different frequency modes were employed to vary the properties of the films, including residual stress. Spectroscopic ellipsometry revealed the changes in thickness of films deposited on silicon substrates.

We evaluated the dissolution behavior of LPCVD nitride, PECVD-LF nitride and PECVD-high frequency (HF) nitride in buffer solutions (pH 7.4 to 12) at RT and 37 °C as shown in Figure 9. Here, three factors (temperature, pH and film characteristics) were considered. The dissolution rate increases with temperature, as expected. Figure 9d shows the pH dependence, which is similar to that observed in the oxides. The kinetics suggest a linear relationship between dissolution rate and pH according to log $r=a + n$ [pH], where n ranges from 0.11 to 0.28 for 37 °C.

We investigated effects of stoichiometry and density. Table 2 shows that the stoichiometry of the LPCVD film is $Si_3N_{3.9}$, while that of the PECVD films is $Si_3N_{4.3}$ (LF) and $Si_3N_{3.3}$ (HF). Figure 9e shows the dependence of the dissolution rate on average film density. The densities are 3.1 g/cm^3 for LPCVD, 3.0 g/cm^3 for PECVD-LF and 2.5 g/cm^3 for PECVD-HF. The results suggest that LPCVD nitride exhibits the lowest dissolution rate, at least partly due to its favorable stoichiometry and high density. PECVD-HF nitride shows the fastest dissolution rate due to its non-stoichiometric chemistry and its low density. The modified reactive diffusion model described previously [16] can provide some utility in capturing the effects of porosity, subject to limitations associated with its approximations. From the results of Figure 9a-c, the reaction constants (k) were found to be 8.0×10^{-8} , 4.5×10^{-7} , and 4.0×10^{-7} s^{-1} for LPCVD nitride, PECVD-LF nitride and PECVD-HF nitride, respectively, in a buffer solution (pH 7.4) at 37 °C using a modified reactive diffusion model where the density of closely packed amorphous nitrides was 3.16 g/cm^3.
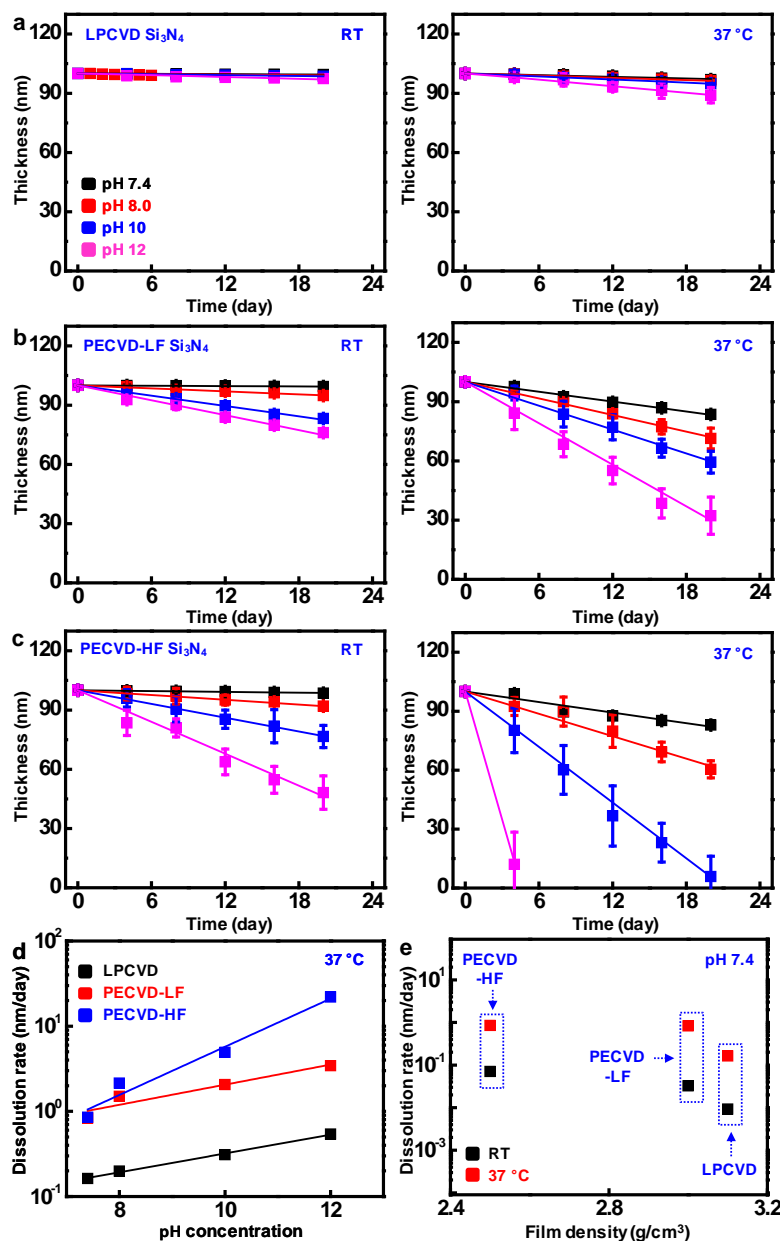
Figure 9: Dissolution Kinetics via Hydrolysis of Various Silicon Nitrides in Aqueous Solutions at Different pH and Temperature

a) Calculated (lines) and measured (symbols) values for the dissolution of Si₃N₄ formed by LPCVD in buffer solutions (black, pH 7.4; red, pH 8; blue, pH 10; magenta, pH 12) at room (left) and physiological (right, 37 °C) temperature. b) Calculated (lines) and measured (symbols) dissolution behaviors of PECVD Si₃N₄ (low-frequency mode) in diverse aqueous solutions with different pH at room (left) and physiological (right, 37 °C) temperature. c) Calculated (lines) and experimental (symbols) results of dissolution study on PECVD Si₃N₄ (high-frequency mode) in aqueous solutions at different pH and temperature. d) Calculated (lines) and experimental (symbols) results of the dependence of dissolution kinetics of silicon nitride films on pH (black, LPCVD Si₃N₄; red, PECVD Si₃N₄ (low frequency); blue, PECVD

21

Si₃N₄ (high frequency)) at physiological temperature (37°C). e) Measured dissolution rate of silicon nitrides as a function of film density in buffer solution (pH 7.4) at room (black) and physiological (red, 37 °C) temperature.

Table 2. Atomic Concentration of Different Silicon Nitrides Measured by XPS
Carbon (C) and fluorine and (F) are considered surface contamination

(%)	Si	N	F	C	x (Si_3N_x)
LPCVD Si_3N_4	36.3	47.8	5.3	10.7	3.9
PECVD-LF Si_3N_4	35.2	50.6	6.2	8.1	4.3
PECVD-HF Si_3N_4	36.9	40.1	11.8	11.2	3.3

5.1.2.3 Dielectric Properties of Transient Inorganic Materials

We investigated the dielectric constants to apply inorganic layers to RF circuits. The parallel plate capacitor was formed to measure the dielectric properties of the interlayers – PECVD oxides, E-beam oxides, SOG, and PECVD nitrides. The thickness of the dielectric layer was 900 nm, and the size of plates was 50 μm by 50 μm. The plate was formed by E-beam evaporation of 300 nm thick Mg layers. The measured dielectric constants were summarized in Table 3.

Table 3. Dielectric Constants and Form Condition of Inogranic Layers in this Study
(Meausred at 10 MHz)

Type of inorganic layer	Measured complex dielectric constant (real, imaginary)	Remark
PECVD SiO_2	4.1, 0.05	Deposited at 350 ⁰C
E-beam SiO_2	5.8, 0.15	
Spin on glass	6.2, 0.2	Cured at 300 ⁰C
PECVD SiN_x	7.3, 0.2	Deposited at 300 ⁰C (mean frequency)
LPCVD SiN_x	*7.9, N/A	*From manufacturer

5.1.3   Contractor will Identify and Measure Key Performance Characteristics of Candidate Metal Conductive Layers for Interconnect and Device Integration

5.1.3.1 Morphological and Electrical Dissolution Behaviors of Biodegradable Metals

We summarize representative dissolution behavior in terms of the change in resistance as a function of time for various metal thin films in DI water and Hanks' solutions (for pH values between 5 and 8) at both RT and body temperature (37 °C) in Figure 10a–g. Changes in thickness with time for dissolution in DI water at RT appear in Figure 10h, i. We found that i) Mg, AZ31B Mg alloy and Zn dissolved much faster than W, Mo, and Fe; ii) the dissolution rate of Mg, Mg alloy, and Zn increase in salt solutions; and iii) the dissolution rate increases with body temperature (between RT and 37 °C) for W, Mo, and Fe, but not significantly for Mg, AZ31B Mg alloy, and Zn.
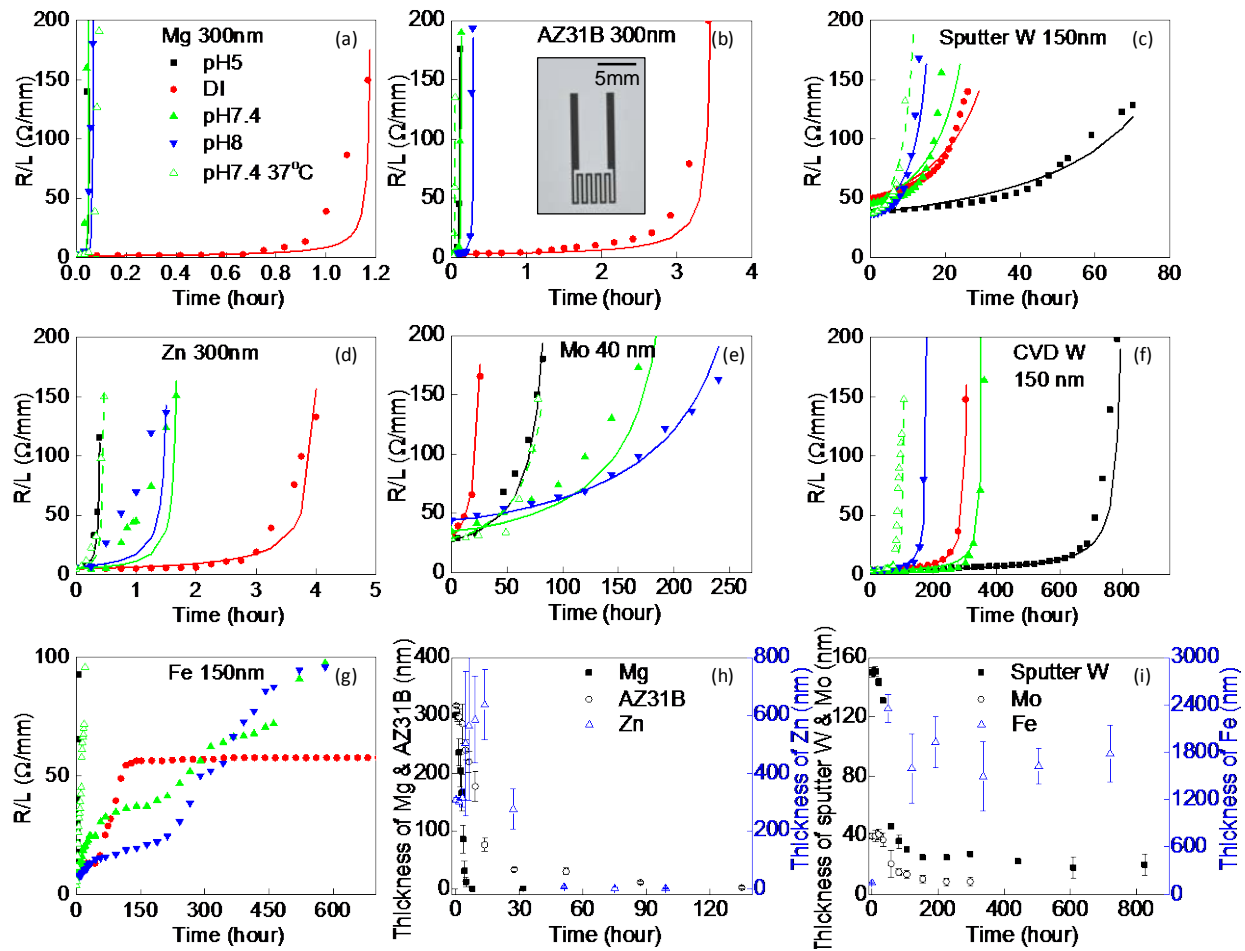
Figure 10: Change in Resistance of Serpentine Thin Traces as a Function of Time during Dissolution in Hanks' Solution (pH 5, 7.4 and 8 at RT and pH 7.4 at 37 °C) and in DI Water

For cases of a) Mg (300 nm); b) AZ31B Mg alloy (300 nm); c) sputter deposited W (150 nm); d) Zn (300 nm); e) Mo (40 nm); f) CVD W (150 nm); and g) Fe (150 nm); a–g) share the same legend. Change in thickness of similar traces as a function of time during dissolution in DI water at RT for cases of h) Mg, AZ31B Mg alloy, and Zn; and i) Mo, Fe and sputter deposited W.

5.1.3.2 Microstructure and Surface Chemistry Associated with Reactive Dissolution of Mg and AZ31B Mg Alloy

The microstructure and surface chemistry for Mg and Mg alloy during the course of dissolution in DI water appear in Figures 11 and 12, respectively. We observed very uniform dissolution for both Mg and AZ31B Mg alloy (Figure 11 and 12a-d). Micropores develop and the surface roughens and becomes uneven as dissolution proceeds and needle-like dissolution products appear (Figure 11 and Figure 12f-g). XPS results are shown in Figure 11 and Figure 12j-k. The assigned binding energies are Mg (49.9eV), Mg-(OH) (50.5 eV) and carbonate (51.5 eV) for Mg 2p; and Mg-O (531.0 eV), Mg-OH (532.1 eV) and carbonate (532.8 eV) for O 1s. The binding energies for AZ31B Mg alloy are Mg (49.5 eV), Mg-(OH) (51.0 eV) and carbonate (52.8 eV) for Mg 2p; and Mg-O (531.0 eV), Mg-OH (532.5 eV) and carbonate (533.5 eV) for O 1s (here '-' represents bond between atom, and p, s, and f represent the orbital. The same notation will be used for the analysis of XPS). The increase in binding energies for hydroxyls and carbonates likely arise from the presence of Al. Surface oxides/hydroxide/carbonates can be found on the film, even before immersion, due to the presence of oxygen, water vapor and carbon dioxide in the atmosphere. During dissolution, the outer surface consists mainly of $Mg(OH)_2$, possibly with a small amount of MgO and carbonates.

The presence of Na^+, Cl^-, PO_4^{3-} and CO_3^{2-} in these solutions can introduce phosphates and carbonates into the surface layer. The TEM bright field images (Figure 11 and Figure 12i) illustrate metallic Mg and needle-like oxide products, consistent with the SEM images. The TEM diffraction patterns and lattice fringes indicate the presence of crystalline MgO, suggesting a possible amorphous nature of the outer $Mg(OH)_2$ layer. These results are consistent with the proposed bi-layer surface oxide structure of bulk Mg dissolved in water or NaCl solution, with a thick outer layer rich in $Mg(OH)_2$ on top of a thin crystalline MgO film. The MgO likely forms immediately after the exposure of a fresh metallic surface to oxygen in the atmosphere. The $Mg(OH)_2$ layer increases in thickness as the dissolution proceeds, due to hydration of the native MgO followed by a dissolution precipitation mechanism at the expense of the base metal.

Figure 11: Evolution of the Microstructure and Surface Chemistry Associated with Dissolution of Mg in DI Water
(a)-(d) optical images; (e)-(h) SEM images with cross-sectional views in the insets; (i) TEM bright field image with diffraction patterns and lattice fringes; (j)-(k) XPS data.

Figure 12: Evolution of Microstructure and Surface Chemistry Associated with Dissolution of AZ31B Mg Alloy in DI Water
(a)-(d) optical images; (e)-(h) SEM images with cross-sectional views in the insets; (i) TEM bright field image with diffraction patterns and lattice fringes; (j)-(k) XPS data.

5.1.3.3 Microstructure and Surface Chemistry Associated with Reactive Dissolution of W and Mo

We described results for dissolution of sputter deposited W and Mo in DI water in Figure 13 and Figure 14. As transition metals in the same column of the periodic table, W and Mo are expected to have similar surface chemistry. The surface morphologies of W and Mo during dissolution are mostly uniform based on the optical observations (Figure 13 and Figure 14a-d). Micropores are evident, however, in SEM results (Figure 13 and Figure 14f-g) and more clearly in the TEM bright field images (Figure 4 and Figure 5i). XPS analysis reveals that the W film has an initial native oxide, mostly WO_3 (Figure 4j-k). As dissolution proceeds, a mixture of oxides (W^{4+}, W^{5+} and W^{6+}) develops at the surface. The thickness of these oxides increases to values larger than 10 nm after ~32 hours, as inferred by the disappearance of the metallic W signal in the XPS data. Further reaction eliminates the W^{4+} and W^{6+} oxides, leaving only the W^{5+} oxide (Figure 13j-k). The oxygen peaks of W in Figure 13k suggest the presence of hydroxide (OH-) and absorbed water at the surface. The assigned binding energies are W (31.8 eV), W^{4+} (32.7 eV), W^{5+} (33.8 eV) and W^{6+} (36.2 eV) for W 4f 7/2; O^{2-} (530.8 eV), OH- (531.9 eV) and H2O (533.2 eV) for O 1s (here f is the orbital). TEM diffraction patterns and lattice fringes also suggest the presence of

WO$_3$ as a dissolution product (Figure 13i). Such a surface structure is similar to that of bulk W materials exposed to an acidic solution, as reported by Lillard et al., [17] where an inner WO$_3$ layer and an outer loosely bound W hydroxide layer occur. As shown in Figure 14j-k, the evolution of surface chemistry for Mo is similar to that for W, with an initial MoO$_3$ native oxide, then a mixture of valence oxides (Mo^{4+}, Mo^{5+} and Mo^{6+}) as dissolution products, with terminal formation of Mo^{5+} oxide after 80 days. The presence of hydroxide and sometimes absorbed water are also observed on the Mo surface based on the XPS O 1s data (Figure 14k). The assigned binding energies are Mo (228.7 eV), Mo^{4+} (229.5 eV), Mo^{5+} (230.9 eV) and Mo^{6+} (233.0 eV) for Mo 3d5/2; O^{2-} (530.7 eV), OH$^-$ (531.8 eV) and H$_2$O (533.0 eV) for O 1s. The TEM results of Mo in Figure 14i support the presence of MO$_3$ and MoO$_2$. These findings are consistent with reported dissolution surface chemistry of bulk Mo materials in aqueous solution [18,19]. Degradation of W and Mo in salt solutions with different pH values follows dissolution patterns similar to those in DI water. The pH can affect the relative concentrations of the various mixed valence surface oxides in ways that can alter the dissolution rate. Due to the solubility of WO$_x$ and MoO$_x$, both W and Mo can slowly degrade in water form micropores (Figure 13 and Figure 14c, g and i).

Figure 13: Evolution of Microstructure and Surface Chemistry Associated with Dissolution of Sputtered Deposited W in DI Water
(a)-(d) optical images; (e)-(h) SEM images with cross-sectional views in the insets; (i) TEM bright field image with diffraction patterns and lattice fringes; (j)-(k) XPS data.
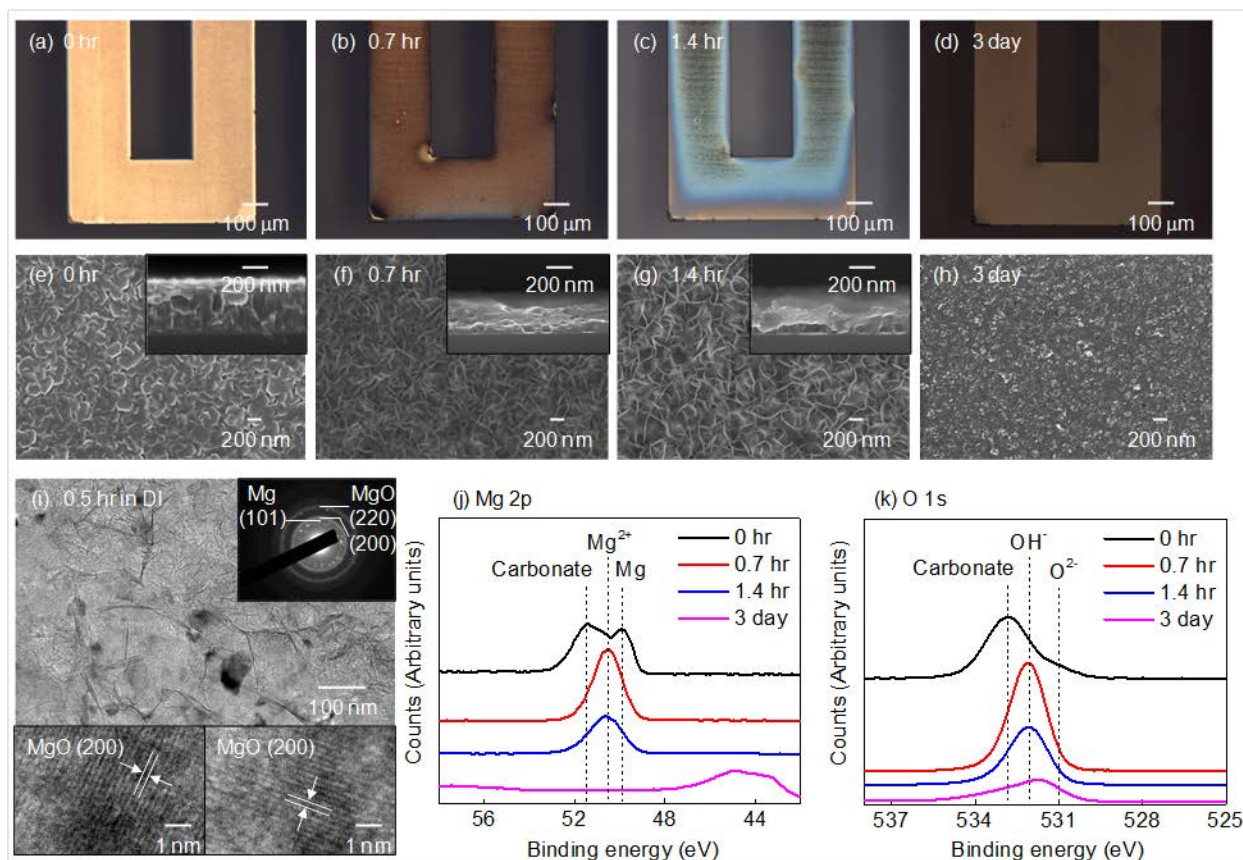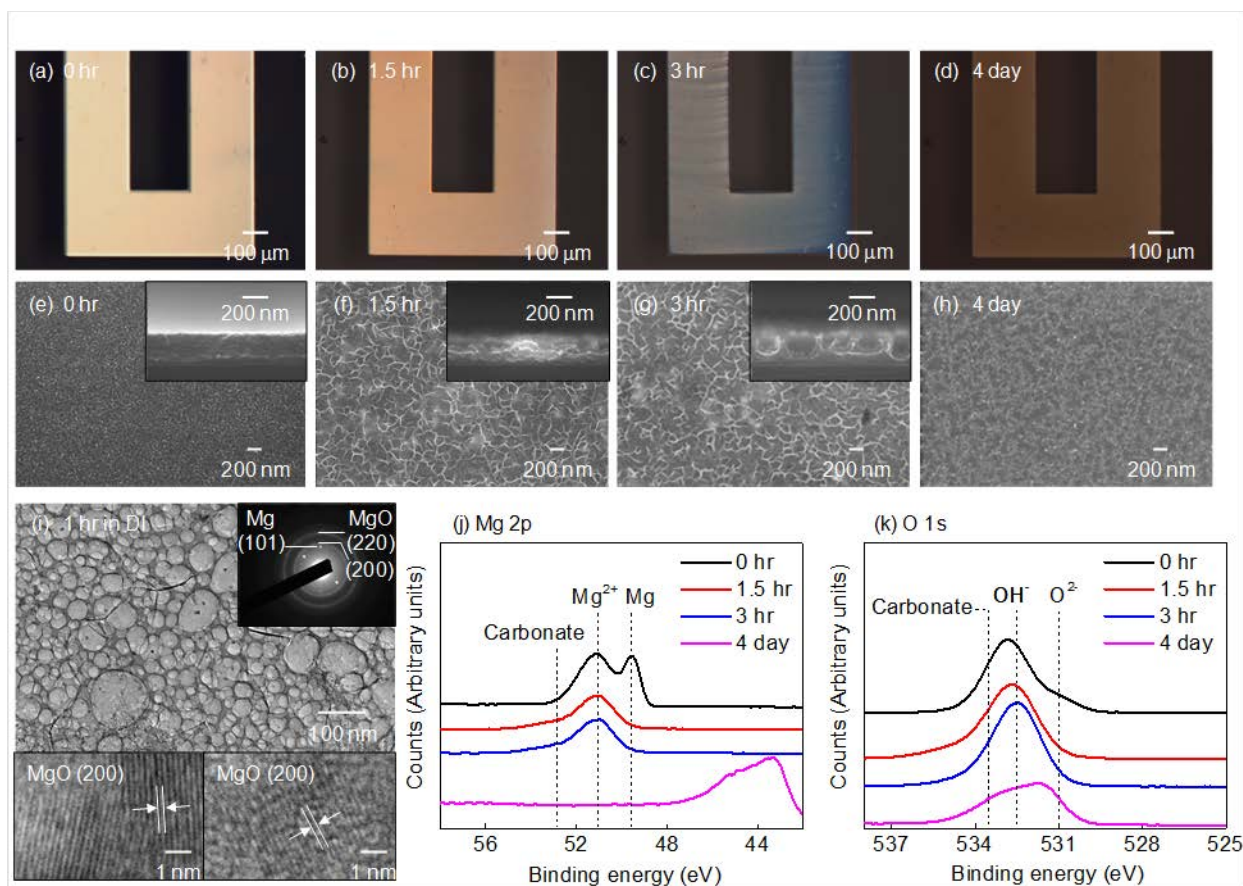
Figure 14: Evolution of Microstructure and Surface Chemistry Associated with Dissolution of Mo in DI Water
(a)-(d) optical images; (e)-(h) SEM images with cross-sectional views in the insets; (i) TEM bright field image with diffraction patterns and lattice fringes; (j)-(k) XPS data.

5.1.3.4 Microstructure and Surface Chemistry Associated with Reactive Dissolution of Zn and Fe

We observed that non-uniform dissolution dominates in the cases of Zn and Fe thin films in DI water (Figure 15 and Figure 16). Pitting nucleates in random locations and then spreads across the films. Such corrosion is commonly observed in bulk samples of Zn and Fe in aqueous solutions. The evolution of surface morphology for Zn is illustrated in Figure 15e-h, where both petal-like and fiber-like dissolution products are observed. Independent of morphology, the surface products are identified to be mainly ZnO and $Zn(OH)_2$ with the occasional presence of a certain amount of carbonates, as the XPS data shows in Figure 15j-k. The assigned binding energies of O 1s are Zn-O (530.4 eV), Zn-(OH) (531.8 eV) and carbonates (530.0 eV). The Zn 2p 3/2 peak (remaining at 1021.8 eV) does not shift in accordance with O 1s as shown in Figure 15j, and therefore cannot be unambiguously separated. The labeled binding energies of Zn 2p in Figure 15j are Zn (1021.6 eV), Zn-O (1021.7 eV) and Zn-OH (1022.4 eV). The TEM diffraction patterns and lattice fringes confirm the presence of ZnO on the surface (Figure 15i). The TEM bright field image also illustrates a porous morphology and a non-uniform distribution of surface oxide, with more ZnO present on the left part of the image (Figure 15i). Dissolution of Zn thin films in Hanks' solutions show similar non-uniform behavior, where the products are also

expected to be mainly ZnO and Zn(OH)$_2$ for bulk Zn materials. Such Zn oxide layers are only partially protective and have relatively high solubility in an aqueous solution. The surface morphologies of dissolution products for the case of Fe appear in Figure 16f-h. The XPS data (Figure 16j-k) suggests that the surface layer is Fe$_2$O$_3$ for Fe 2p and hydroxide for O 1s, with Fe 2p 3/2 for Fe (706.9 eV) and O 1s for Fe$_2$O$_3$ (529.8eV) and hydroxide (531.2 eV). The TEM diffraction patterns and lattice fringes (Figure 16i) indicate the presence of Fe$_3$O$_4$, which is a common corrosion product that forms the hydroxide in the presence of excessive oxygen. The presence of Fe oxides can help passivate the propagation of pits and simultaneously reduce the dissolution rate. Although Zn also shows non-uniform patterns of dissolution, the facile initiation of pits and high reaction rates eliminate plateaus in dissolution. The degradation behavior of Fe in Hanks' solution is similar to that in DI water except at pH 5, for which uniform dissolution and the absence of obvious surface oxides are observed, resulting from the acidic environment.

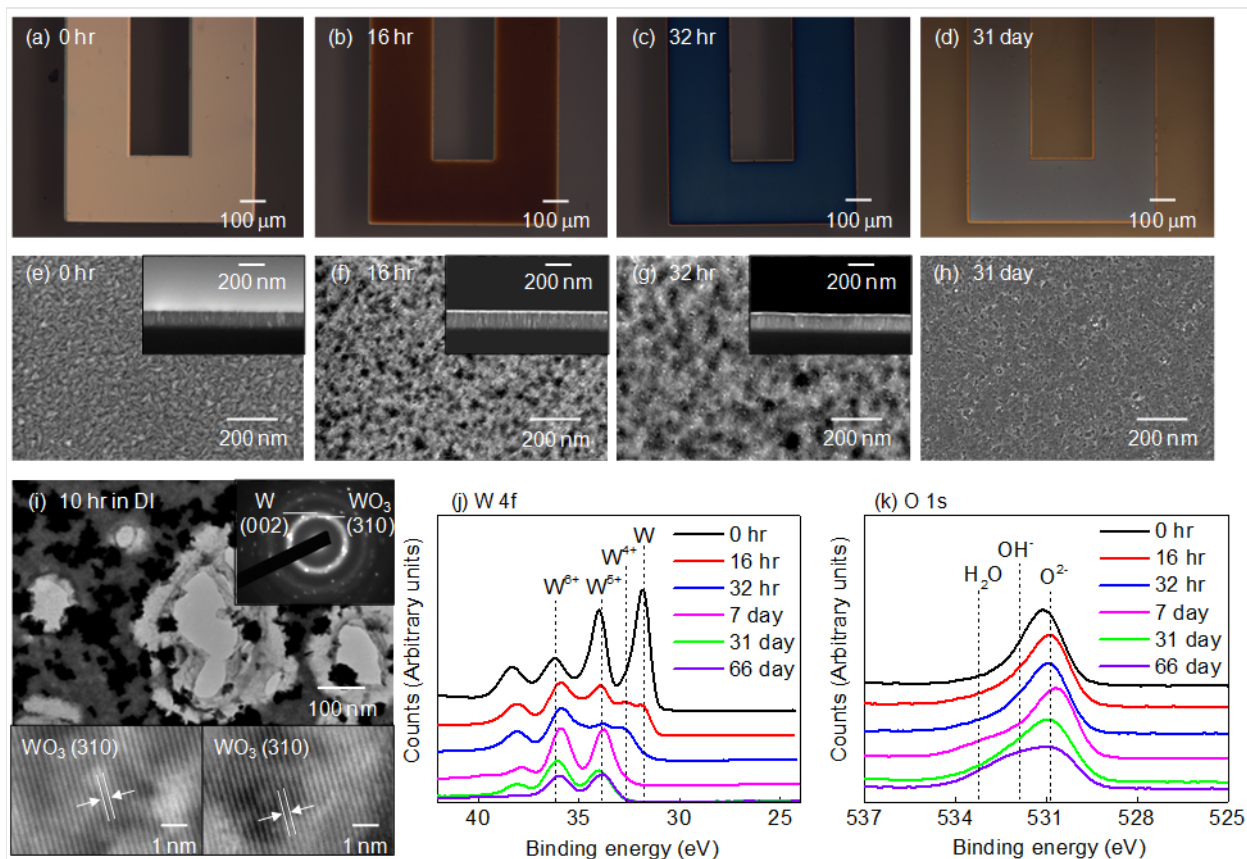**Figure 15: Evolution of Microstructure and Surface Chemistry Associated with Dissolution of Zn in DI Water**

(a)-(d) optical images; (e)-(h) SEM images with cross-sectional views in the insets; (i) TEM bright field image with diffraction patterns and lattice fringes; (j)-(k) XPS data.
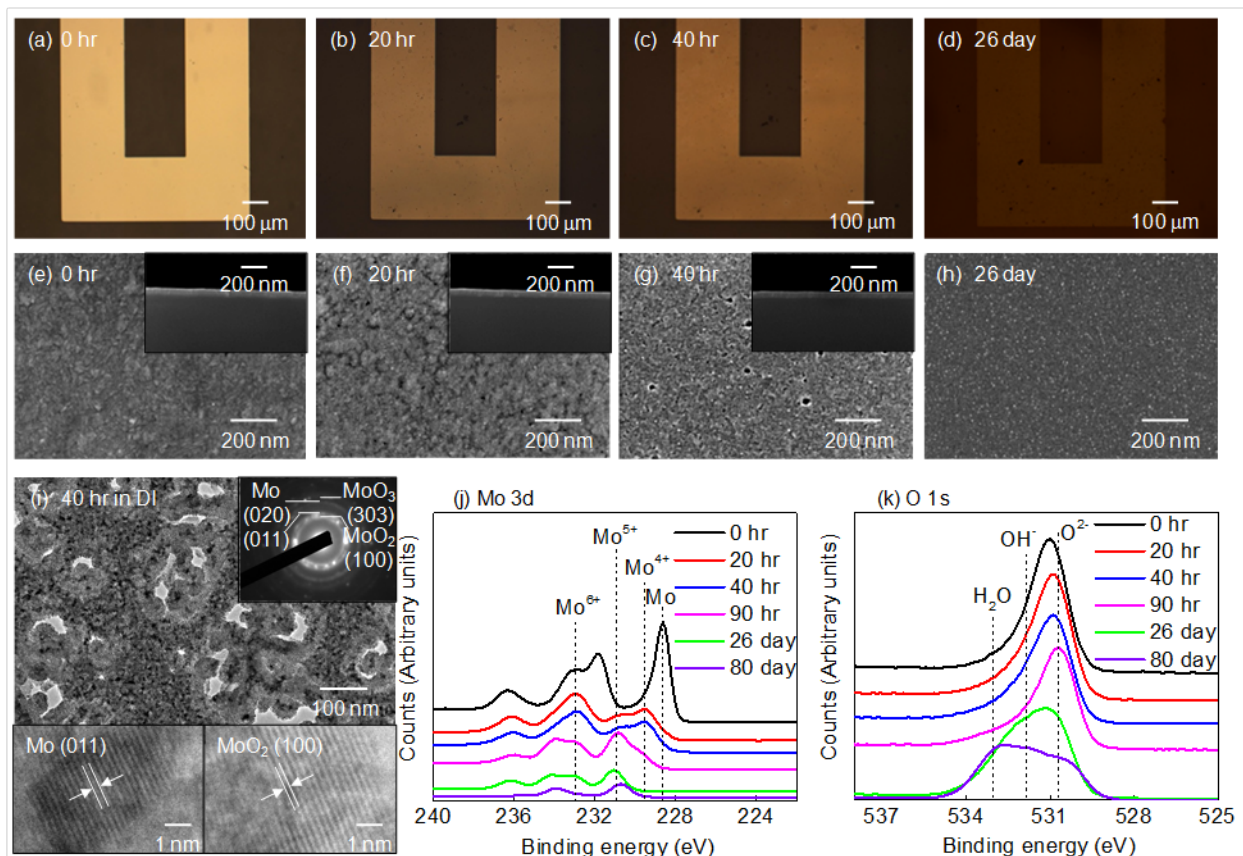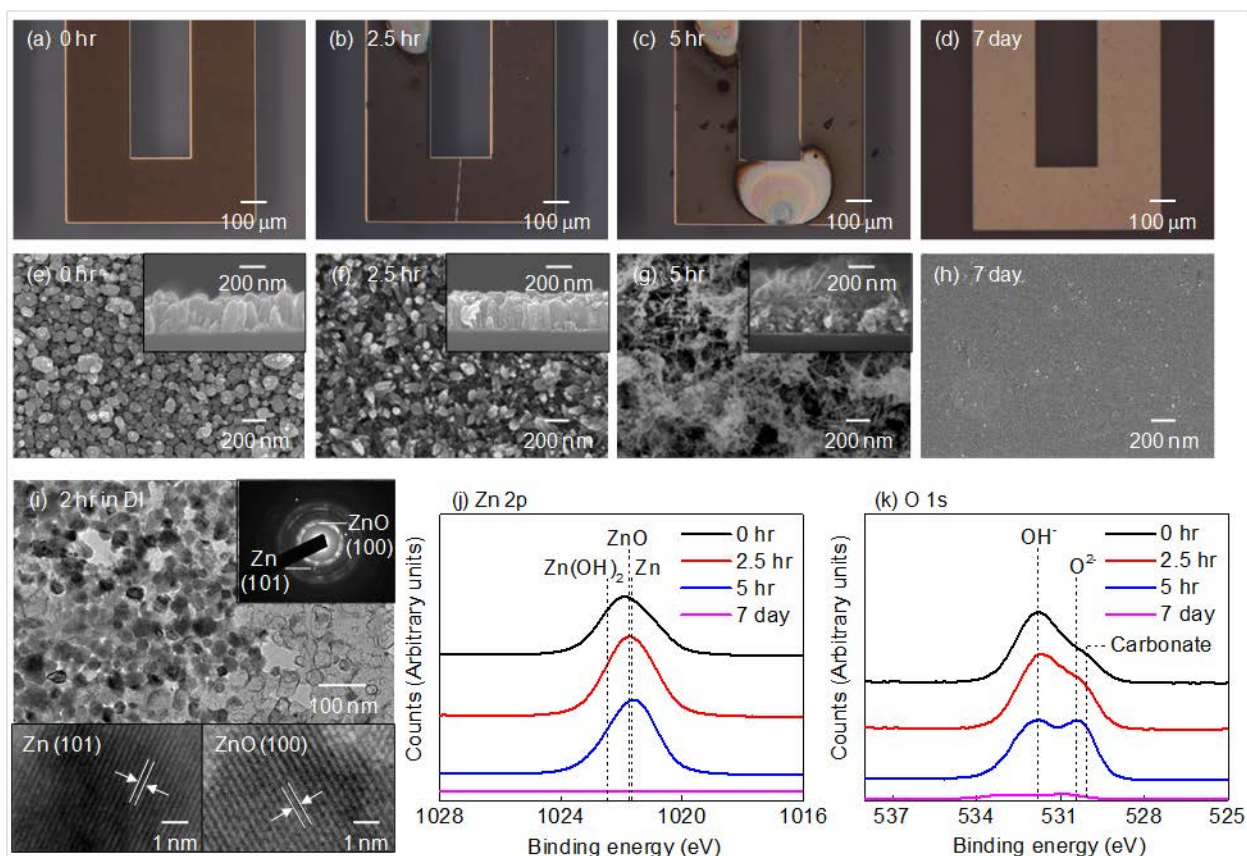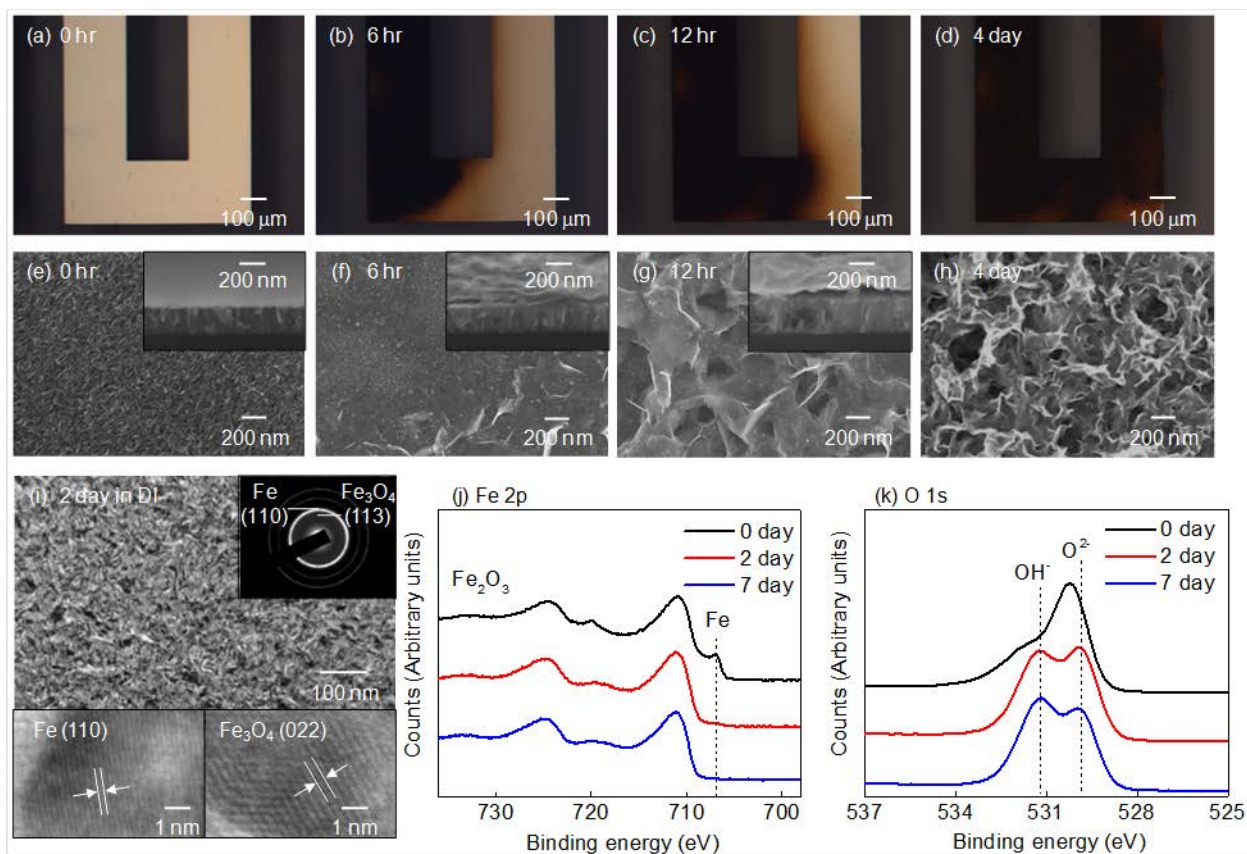
Figure 16: Evolution of Microstructure and Surface Chemistry Associated with Dissolution of Fe in DI Water
(a)-(d) optical images; (e)-(h) SEM images with cross-sectional views in the insets; (i) TEM bright field image with diffraction patterns and lattice fringes; (j)-(k) XPS data.

5.1.3.5 Characteristic of Biodegradable Metals as an Interconnection in Electrical Device

We demonstrated the use of biodegradable metal as an interconnect in electrical devices such as n-MOSFET. The geometry of the devices, which are constructed on silicon-on-insulator (SOI) wafers, is illustrated in Figure 17a, where the metal layers were Mg (300 nm), AZ31B Mg alloy (300 nm), Zn (300 nm), W (150 nm) and Mo (80 nm), respectively, and the gate dielectric was 100 nm of PECVD SiO_2. The lengths (*L*) and widths (*W*) of the channels in all cases are 50 μm and 400 μm, respectively. The typical on/off ratios and mobilities are $>10^4$ and 250 cm^2 V^{-1} s^{-1}, respectively, regardless of the type of metal. The data suggests negligible effects of contact resistance, partly due to the relatively large *L*. Detailed studies of the contacts lie beyond the scope of the present work. Data related to the functional degradation of these MOSFETs induced by immersion in DI water appear in Figure 17b-f. Due to the relatively fast dissolution rate for the metals ($<\sim 1X10^4$ nm/day) compared to silicon and PECVD silicon oxide ($\sim 0.01^{-1}$ nm/day), the degradation in functionality mainly results from the loss of contacts as the dissolution proceeds. As seen in Figure 17, MOSFETs with Mg, AZ31B alloy and Zn contacts cease to function after ~2-8 hours while those with W and Mo exhibit stable operation for ~12 hours and ~25 hours, respectively. These results are consistent with expectations based on the dissolution rates.
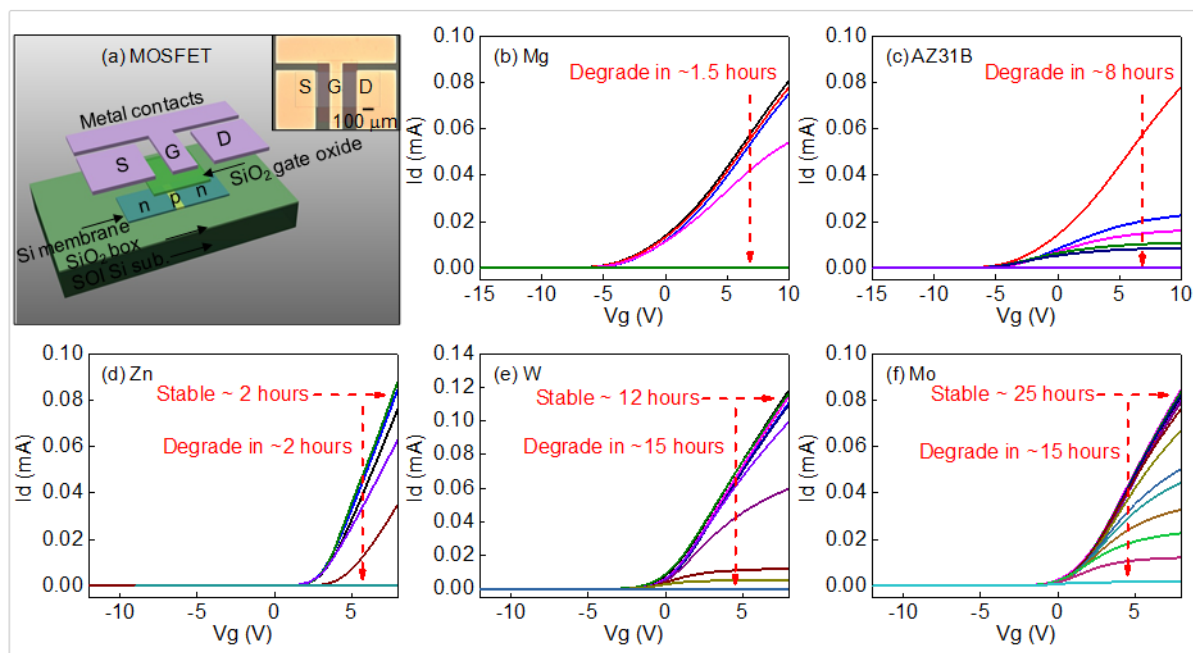
Figure 17: Geometry of an N-channel MOSFET
(a) with a top view optical micrograph in the inset (b)-(f) functional degradation of n-channel MOSFETs, as evaluated through measurements of the drain current (Id) as a function of gate voltage (Vg) for a drain bias (Vd) of 0.2 V, with transient metal contacts: Mg, AZ31B Mg alloy, Zn, W and Mo respectively. (The lines with different color in b-f represents the sequential measurement at every 20 min for b, d, and 2 hour for c, e, f.)

5.1.4   Contractor will Identify Key Control Parameters for Tuning the Water Permeability, Dissolution Kinetics, and Dimensional Change due to Swelling in Addition to Critical Electrical Properties affecting Electronic and/or RF Performance of the Studied Conductors

This item was associated in 5.1.1, 5.1.2, and 5.3.1 and summarized together at each part.

5.2   Design and Demonstrate Inorganic Substrates Systems and Encapsulants

5.2.1   Contractor will Design and Demonstrate Controllable Dissolution of an Inorganic-based Substrate System and Encapsulation Strategy with Application Appropriate Transience Times and Dielectric Properties

5.2.1.1 Fabrication of Transient Device with Biodegradable Metal Substrates

We proposed the strategy to fabricate transient devices on inorganic metal substrates which allow PECVD or SOG based inorganic encapsulations. Figure 18a illustrates a fabrication strategy for transient n-channel MOSFETs on biodegradable metal foils as an example process. The fabrication starts with laminating the foils Fe, Mo, W, and Zn, ~10 μm thick (Goodfellow, USA) on glass slides coated with PDMS (Dow Corning Co., USA) as temporary supports during device processing. A layer of SiO_2 (~1 μm) deposited by PECVD on the foils electrically

Approved for public release; distribution unlimited.

isolates the substrates from the device layers. A layer of SOG (Filmtronics Inc., USA), described in detail subsequently, serves as an adhesive layer for transfer printing Si NMs with patterns of dopants introduced by diffusion of phosphorus from a solid source at 950 °C. RIE (Plasmatherm, USA) with SF_6 gas patterns the Si into areas that match the desired device layouts. PECVD, E-beam evaporation and photolithography form patterned gate dielectrics (SiO_2, ~100 nm) and metal electrodes (Mg, ~300 nm). Such processing, although trivial on metal foils, would not be possible with biodegradable polymer substrates. Figure 18b shows an image of an Fe foil with thickness of ~10 μm (left) and a microscope image (right). Figure 18c shows an array of n-channel MOSFETs on this substrate. The thinness of the foil leads naturally to a low bending stiffness that taken together with its physical toughness enables mechanical flexibility. This flexibility is important for many classes of biomedical devices (Figure 19a). Figure 19b presents examples of use in scenarios that could benefit from magnetic positioning techniques in deployment.
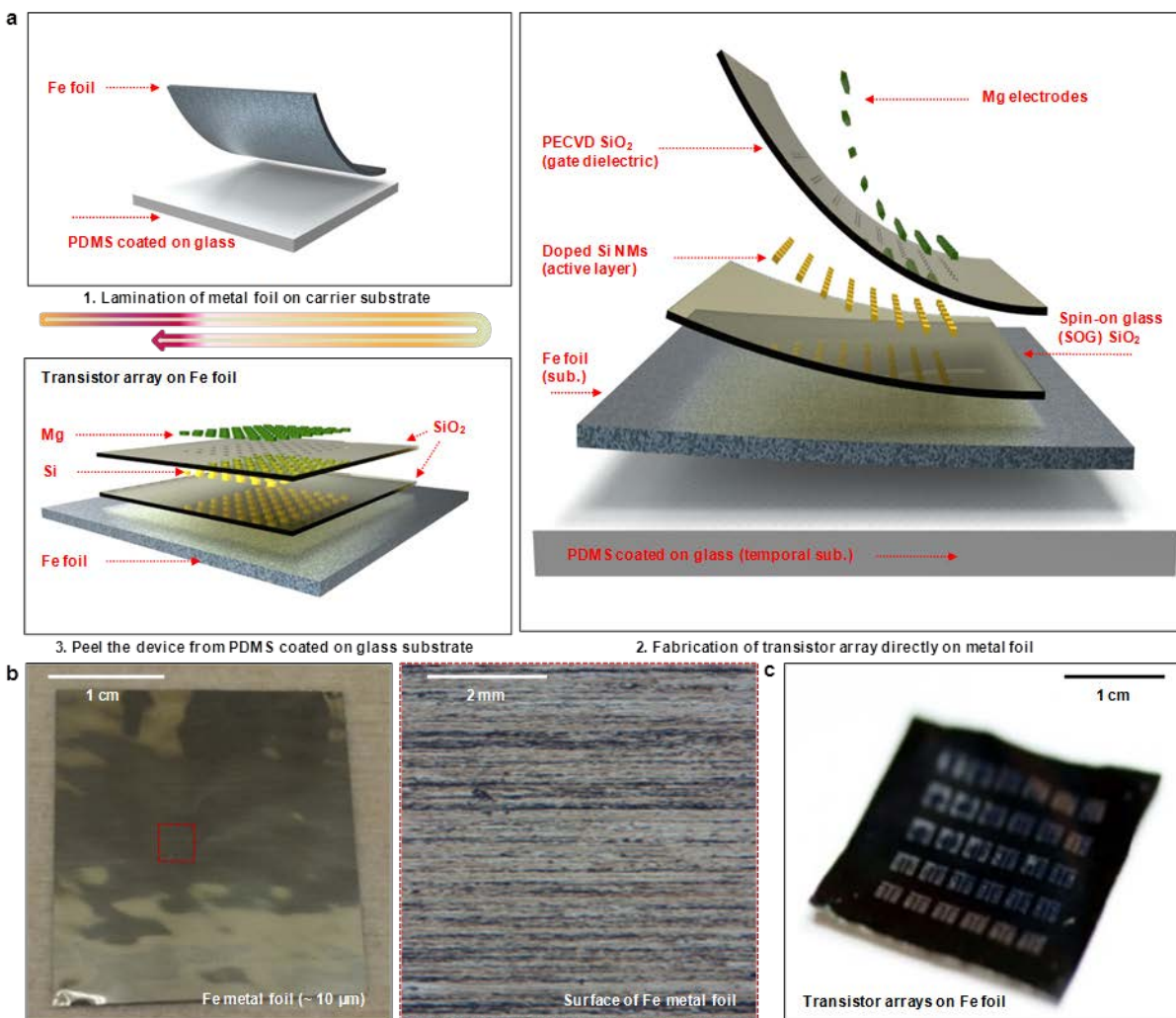
Figure 18: Fabrication Procedures for Transient N-channel MOSFET Array on a Biodegradable Fe Foil

(a) Lamination of a Fe foil on a PDMS coated glass substrate (top left). Exploded-view schematic illustration of a transient n-MOSFET (right). Detachment from the PDMS/glass substrate yields a free-standing system (bottom left). The materials include silicon nanomembranes (Si NMs; semiconductor), thin magnesium (conductor) films, spin-on glass (SOG, dielectrics), silicon dioxide (SiO_2, dielectric) and Fe foil (substrate), all of which are biodegradable. (b) Image of ~10 μm thick Fe and Mo foils before fabrication (left), including microscope image (right). (c) Image of array of n-channel MOSFETs fabricated on the Fe foil.

33
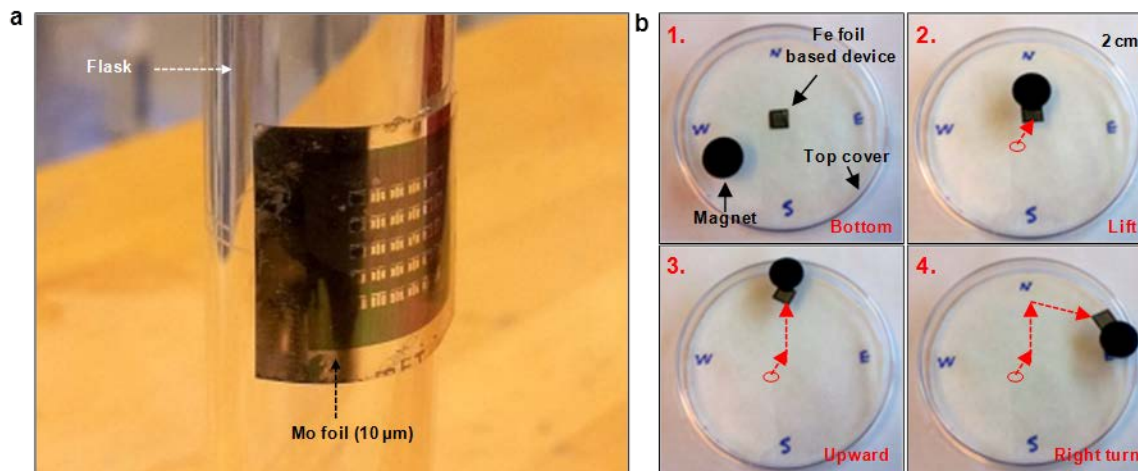
Figure 19: Characteristics of Metals Substrates Based Device
a) Flexible use is available because metal substrate is thin enough to lower flexible modulus. b) Possibilities of electromagnetic remote control of Fe substrate devices.

5.2.1.2 Passivation of Metal Foil Substrates

We tested the three different kinds of passivation materials for electrical isolation between the metal foil substrate and device. The PECVD SiO_2 and SiN_x are suitable to give the passivation layer due to their fast deposition rate and lower process temperature. Also spin-on glass is one good candidate with superior coverage. The Mg resistor (~300 nm) was formed on Mo foil passivated with PECVD SiO_2 and PECVD SiN_x, ranging in thickness from 100 nm to 300 nm, and spin-on glass (~300 nm). If the resistance of the Mg resistor on Mo foil is the same as that on a glass substrates, there is no leakage through the metal foil substrate and it can be concluded that the resistor is well passivated. Table 4 proposed the materials and thickness of the resistor which gave the same performance on insulator substrates, so they are usable as a passivation layer for the metal foil substrate.

Table 4. Materials and Thickness for Passivation of Conductive Metal Substrates

Type of inorganic layer	Available thickness	Remarks
PECVD SiO_2	> 200 nm	100 nm, 200 nm and 300 nm were tested.
PECVD SiN	> 100 nm	100 nm, 200 nm and 300 nm were tested.
Spin on glass	300 nm	300 was tested.

5.2.1.3 Dissolution Kinetics of Biodegradable Metal Substrates

We studied the dissolution kinetics of metal as a thin film since the thickness, grain structure and surface morphology can potentially dictate the kinetics of hydrolysis. We observed the fully transient behavior of an integrated system with a representative device, the transient n-MOSFETs on a Mo foil (~ 5 um). Figure 20a shows the transience of the integrated system at various times for partial immersion in a PBS (pH 7.4 at 90 °C). Full dissolution of the foil occurs after 25 days under these conditions; the other materials dissolve at different rates. The dissolution behavior of other metal foil substrates are shown in Figure 20b. The changes in film thickness of Mo, Zn, Fe, and W films in PBS (pH 7.4 at 37 °C) are 0.02, 3.5, 0.08 and 0.15

μm/day, respectively. The dissolution rates of thin films of these metals in Hanks' solution at room temperature are 0.005, 7.2, 0.005, and 0.19 μm/day, which are comparable to the results for the foils. Figure 20c shows thickness profiles of Mo foils during the dissolution tests; the metal foils disappear in a uniform fashion without significant changes in surface morphology.
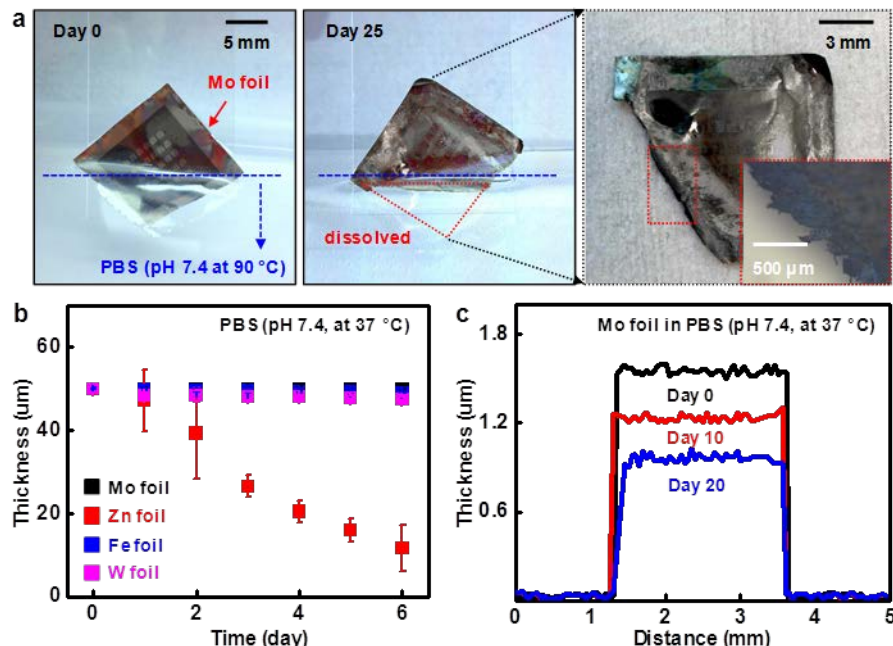
Figure 20: Dissolution of Various Metal Foils

a) Sequential images collected at various stages of dissolution of an array of transistors on a Mo foil (~5 μm) partially immersed in a PBS (pH 7.4) at 90 °C. The device in its initial state (left) and partially dissolved after 25 days (middle). Magnified (right) and microscope (inset) images show full dissolution in immersed areas and partial degradation of Mg electrodes by vapor in an adjacent region. b) Measured dissolution kinetics of metal foils (initial thickness ~50 μm) in PBS (pH 7.4) at 37 °C (black, Mo; red, Zn; blue, Fe; magenta, W).

5.3   Demonstration and Integration of Transient Components

5.3.1   Contractor will demonstrate a Variety of Passive and Active Devices in a Functional Circuit with Operation in a Realistic RF Band to Evaluate Practical Performance of Encapsulants and Substrates

5.3.1.1 Demonstration and Characterization of Active and Passive Devices as an Integrated System

We demonstrate the fabrication strategy of Section 5.2.1.1 with active and passive devices on various kinds of metal substrates and characterize their electrical function including RF characteristics. We described SEM images of an array of transistors and diodes, respectively, with magnified views in the inset (left), and electrical properties (right) in Figure 21a, b. A typical n-channel MOSFET as shown here consists of a doped Si NM (~300 nm, active layer), a layer of PECVD SiO_2 (~100 nm, gate dielectric), Mg electrodes (~300 nm, source/drain/gate contacts) on Fe, with channel length and width of ~30 μm and ~600 μm, respectively. Current-voltage characteristics of a representative device measured at different gate biases appear in the right frame of Figure 21a. Figure 21b shows an image of an array of PIN diodes, each of which consists of a doped Si NM (~200 nm) and Mg electrodes (~300 nm) all on a Zn foil (~10 μm), with typical electrical characteristics (right).

We also demonstrated RF passive devices - capacitors (Figure 21c) and inductors (Figure 21d). Parallel plate capacitors with various lateral dimensions (left, black, 150 μm × 150 μm; red, 250 μm × 250 μm; blue, 400 μm × 400 μm; green, 550 μm × 550 μm) can be formed with SiO_2 (~900 nm) as the dielectric and Mg as the electrodes on Mo foils (~10 μm). Capacitances (Figure 21c, right) and Q factors (Figure 22a) in the frequency range of 0 to 25 GHz exhibit trends and values that are comparable to those of otherwise similar devices on biodegradable polymer substrates. Spiral inductors with two or three turns (Figure 21d, left) constructed using Mg traces and SiO_2 (~900 nm) as an interlayer dielectric can be formed on Mo foils (~10 um). We found that the resonance frequencies and Q factors (Figure 21d, right; Figure 22b) have values that differ from those of devices on polymers. This is likely due to parasitics associated with the conductive substrate. Such effects must be considered in the overall design of RF systems.
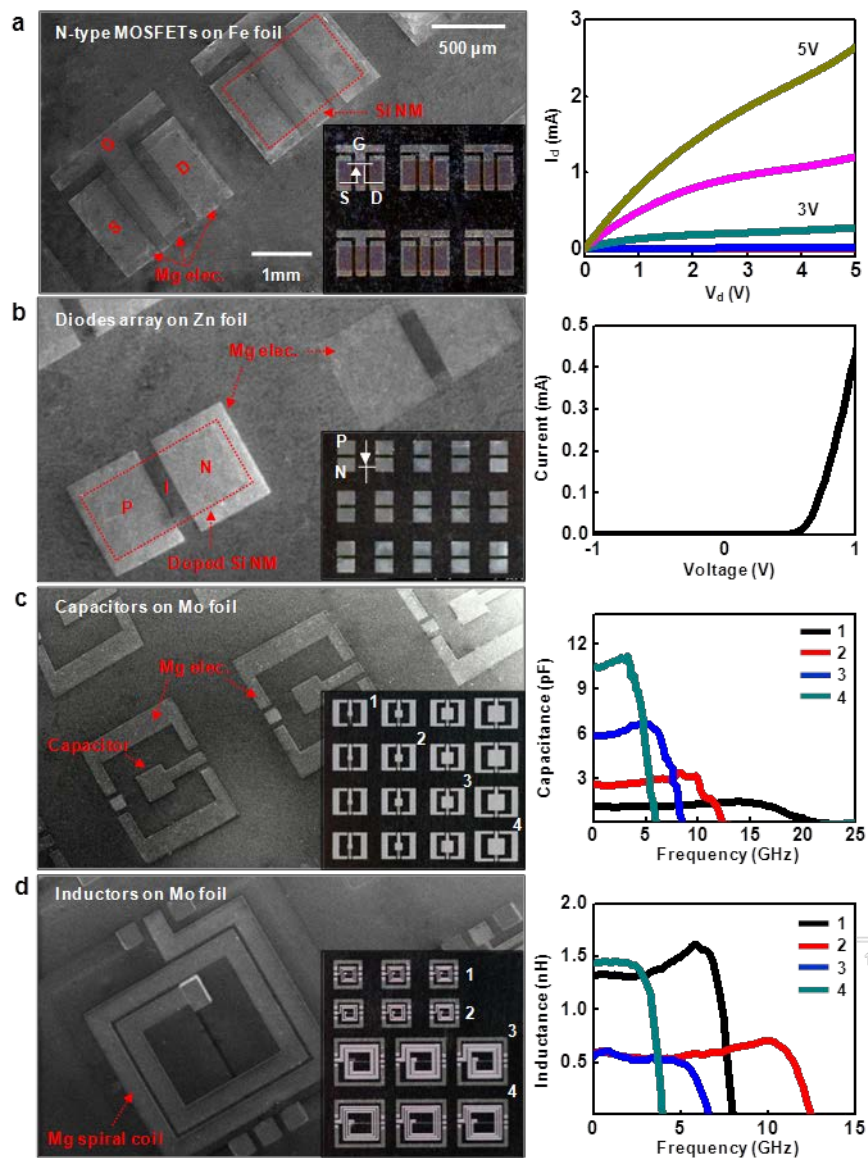
Figure 21: Images and Electrical Properties of Diverse Transient Electronic Devices on Various Biodegradable Metal Foil Substrates

a) SEM and optical microscope image (inset) of an array of n-MOSFETs on Fe foil (~10 μm thick) (left); I-V characteristics of a representative device (right). The channel length L and width W are 30 μm and 600 μm, respectively. The mobility (linear regime) is ~400 cm^2/V·s. b) Transient PIN diode on a Zn foil (~10 um thick) observed by SEM and optical microscope (left and inset). Current-voltage characteristics are typical of PIN diodes (right). c) SEM and optical images of capacitors with different sizes, built using Mg electrodes (top/bottom) and PECVD SiO$_2$ dielectrics on Mo foil (~10 μm thick) (left). Measured capacitance as a function of frequency up to ~25 GHz. The overlap area in these metal-insulator-metal (MIM) capacitors is 150 μm × 150 um (1, black), 250 μm × 250 μm (2, red), 400 μm × 400 μm (3, blue) and 550 μm × 550 μm (4, green). d) SEM and microscope images (inset) of planar spiral coils on a Mo foil substrate (~10 μm) (left). Mg layers provide bottom (~300 nm) and top (~3.5 μm) electrodes, and a PECVD SiO$_2$ layer (~900 nm) serves as interlayer dielectric. Inductance as a function of frequency from 0 to 15 GHz (right). The number of turns (n), outer diameter (d) and metal

37

width/space (w/s) of these spiral coils are 3, 440 µm, 20/20 µm (1, black); 2, 440 µm, 40/20 µm (2, red); 2, 1 mm, 100/20 µm (3, blue); 3, 1 mm, 50/20 µm (4, green).
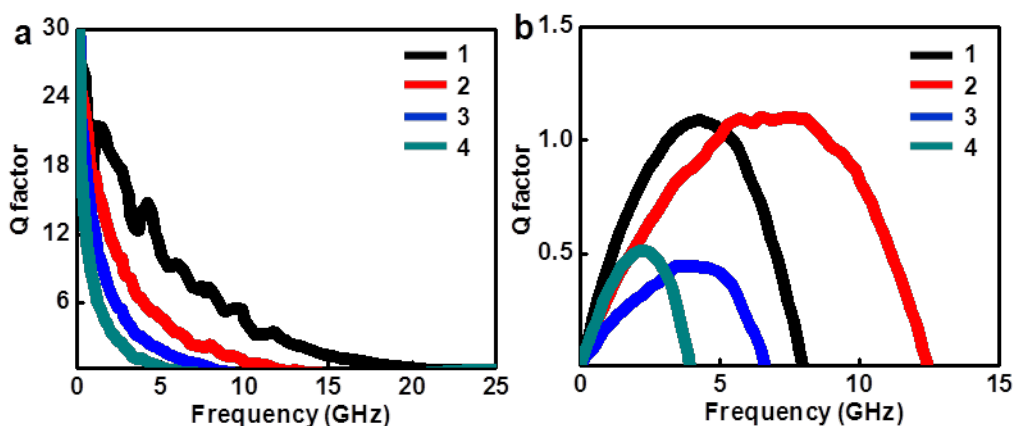

Figure 22: Q factors of a) Capacitors and b) Inductors described in Figure 21c,d

5.3.2   Contractor will demonstrate Control over the Full Integrated System's Transient Time over a Range of Application-appropriate Time Scales (minutes to months) in Both Aqueous Environments under Study

5.3.2.1 Demonstration of Transience Behavior of Integrated System

We summarize the effects of transience by hydrolysis on the electrical function of devices on metal foils in Figure 23. We fabricated systems in geometries similar to those of Figure 21 with extended electrodes (see insets in Figures 23a and b). This allows remote measurements while immersed in DI water at room temperature. Figure 23a illustrates transfer curves of Si n-MOSFETs at $V_d = 0.1$ V (left), and drain current (I_d, right). The results indicate stable operation for ~5 hours, followed by a rapid loss of function due to dissolution of the Mg electrodes. Measurements on transient Si PIN diodes present similar behaviors, as shown in Figure 23b. The cases of transient capacitors and inductors evaluated at 10 MHz appear in Figure 23c, d. Here, different thicknesses of a MgO encapsulation layer provide two-stage kinetics: the first stage (stable operation) is defined by dissolution of the encapsulants (e.g. MgO in this case) and/or permeability of them; the second stage (rapid degradation) is determined by hydrolysis of device materials (mainly the Mg electrodes). After electrical properties degraded fast with dissolution of Mg electrode, the individual component dissolves their own dissolution rates [6].
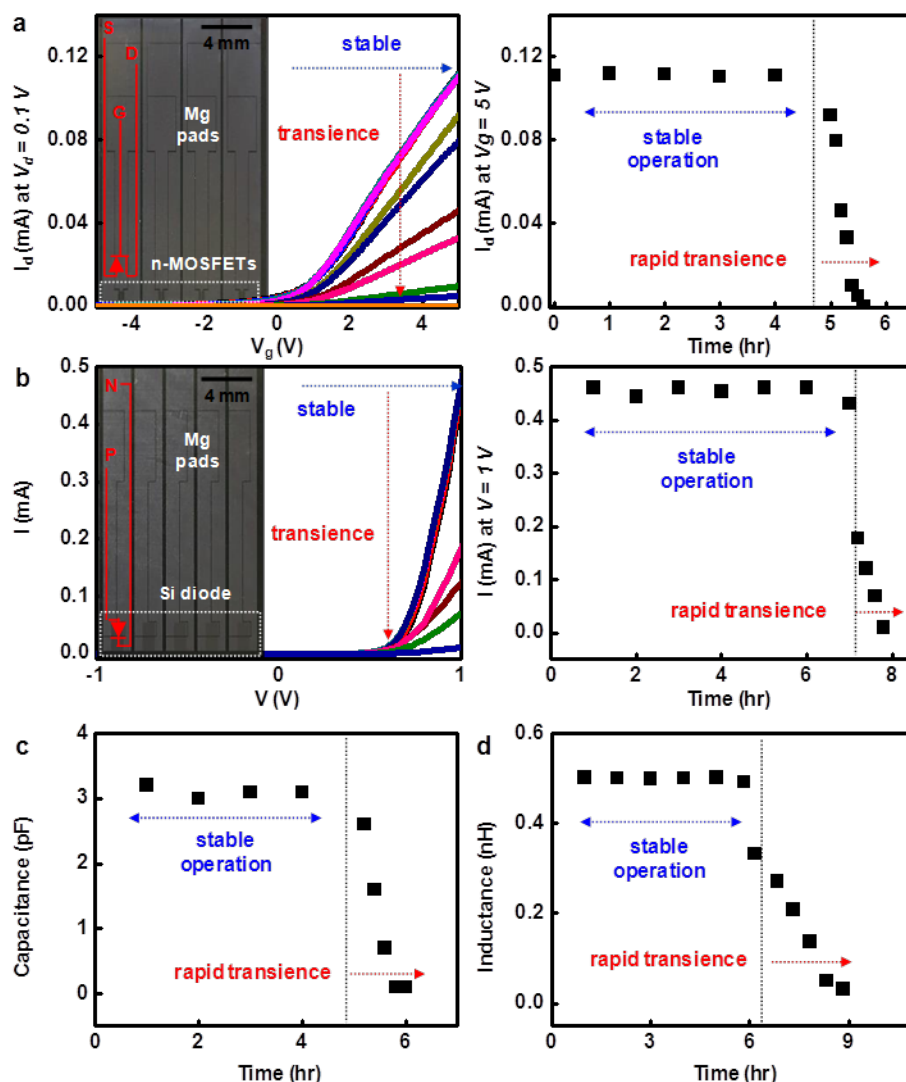
Figure 23: Measurements of Transience at the Device Level

a) Measured drain currents (at V_d = 0.1 V) of typical n-MOSFET (left); image in the inset. The drain current I_d at V_g = 0.5 V as a function of time (right). b) Changes in current in a Si PIN diode (left; image of device in inset). Measured current changes (at V = 1 V) as a function of time (right). c) Measured capacitance of a MIM capacitor as a function of time. d) Measured degradation in inductance of a Mg spiral inductor. In all cases, the systems were encapsulated in MgO (1 - 3 μm) and immersed in DI water at room temperature. The transience shows two-step kinetics involving stable operation for several hours, followed by rapid degradation. The encapsulation layers and the Mg electrodes define the first and second time frames, respectively.

6.0   Conclusion

6.1   Deliver Data in Accordance with CDRLs A001-A004

We have submitted the monthly reports as planned.

6.2   Report Detailing the Growth Methods, Conditions, and other Tunable Properties that Govern the Transience Properties of the Studied Substrates and Metals

We performed the dissolution studies of various oxides and nitrides made by different kinds of growth/deposition methods, which yield dissolution tunability properties in the films. We also studied the dissolution of biodegradable metals as thin films and free-standing foils for transient electrodes and inorganic substrates.

6.3   Five Substrates with Various Transience Times (ranging from minutes to months) and Sufficient Electrical Insulation and Mechanical Stability Properties for use in Flexible, in Vivo, Applications

We proposed five different classes of biodegradable metals (Mg, Mo, Fe, W, Zn) and investigated their range of different transience times. We demonstrated that PECVD SiO_2, SiN_x and SOG provide enough electrical isolation from the conductive metal substrates by demonstrating the functional active and passive devices. These films are available for flexible and in-vivo applications when insulated using SiO_2 or SiN_x passivation layers or possibly other degradable polymers, which can give another tunability of dissolution rates.

6.4   Test Data and Documentation of Electrical, Mechanical, and Transience Performance and Characteristics of the Transient Circuit Components before and after Integration with the Proposed Substrates and Encapsulating Layers

We demonstrated the fabrication of transistors, diodes, capacitors, and inductors on various metal substrates with reasonable electrical functions. The integrated system was also investigated with metal substrates and inorganic encapsulants such as MgO, SiO_2 and SiN_x. The integrated system had good mechanical stability and exhibited two-stage transience.

6.5   Test Data and Documentation of Control over the Fully Integrated System's Transience and Performance over a Range of Application-appropriate Time Scales (minutes to months) in both Aqueous Environments under Study

We provided the transience and performance of a fully integrated system through the demonstration of transistors, diodes, capacitors, and inductors. The operating time of transient devices inside the aqueous solution was controllable through the combination of degradable organic layers with the single or multiple inorganic layers.

7.0   References

[1]   P. P. Mueller, S. Arnold, M. Badar, D. Bormann, F.-W. Bach, A. Drynda, A. Meyer-Lindenberg, H. Hauser, M. Peuster, *J. Biomed. Mater. Res., Part A* **2012**, 100A, 2881.
[2]   Z. Li, X. Gu, S. Lou, Y. Zheng, *Biomaterials* **2008**, 29, 1329.
[3]   N. Erdmann, N. Angrisani, J. Reifenrath, A. Lucas, F. Thorey, D. Bormann, A. Meyer-Lindenberg, *Acta Biomater.* **2011**, 7, 1421.
[4]   S.-W. Hwang, J.-K. Song, X. Huang, H. Cheng, S.-K. Kang, B.H. Kim, J.-H. Kim, S. Yu, Y. Huang, J.A. Rogers, *Adv. Mater.* DOI: 10.1002/adma.201306050.
[5]   S.-W. Hwang, H. Tao, D.-H. Kim, H. Cheng, J.-K. Song, E. Rill, M. A. Brenckle, B. Panilaitis, S. M. Won, Y.-S. Kim, Y. M. Song, K. J. Yu, A. Ameen, R. Li, Y. Su, M. Yang, D. L. Kaplan, M. R. Zakin, M. J. Slepian, Y. Huang, F. G. Omenetto, J. A. Rogers, *Science* **2012**, 337, 1640.
[6]   C. Dagdeviren, S.-W. Hwang, Y. Su, S. Kim, H. Cheng, O. Gur, R. Haney, F.G. Omenetto, Y. Huang, J.A. Rogers, *Small* **2013**, 9, 3398.
[7]   L. Yin, H. Cheng, S. Mao, R. Haasch, Y. Liu, X. Xie, S.-W. Hwang, H. Jain, S.-K. Kang, Y. Su, R. Li, Y. Huang, J.A. Rogers, *Adv. Funct. Mater.* **2014**, 24, 645–658.
[8]   S.-W. Hwang, G. Park, H. Cheng, J.-K. Song, S.-K. Kang, L. Yin, J.-H. Kim, F.G. Omenetto, Y. Huang , K.-M. Lee and J.A. Rogers, *Adv. Mat.* **2014**, 26, 1992.
[9]   S.-K. Kang, S.-W. Hwang, H. Cheng, S. Yu, B.H. Kim, J.-H. Kim, Y. Huang, J.A. Rogers, *Adv. Funct. Mater.* DOI: 10.1002/adfm.201304293.
[10]   S.-W. Hwang, G. Park, C. Edwards, E.A. Corbin, S.-K. Kang, H. Cheng, J.-K. Song, J.-H. Kim, S. Yu, J. Ng, J.E. Lee, J. Kim, C. Yee, B. Bhaduri, Y. Su, F. G. Omennetto, Y. Huang, R. Bashir, L. Goddard, G. Popescu, K.-M. Lee, J.A. Rogers, *ACS Nano* DOI: 10.1021/nn500847g.
[11]   S.-W. Hwang, D.-H. Kim, H. Tao, T.-I. Kim, S. Kim, K.J. Yu, B. Panilaitis, J.-W. Jeong, J.-K. Song, F.G. Omenetto, J.A. Rogers, *Adv. Funct. Mater.* **2013**, 23, 4087.
[12]   S.-W. Hwang, X. Huang, J.-H. Seo, J.-K. Song, S. Kim, S. Hage-Ali, H.-J. Chung, H. Tao, F.G. Omenetto, Z. Ma, J.A. Rogers, *Adv. Mater.* **2013**, 25, 3526.
[13]   K. G. Knauss, T. J. Wolery, *Geochimica et Cosmochim. Acta* **1988**, 52, 43.
[14]   W. A. House, L. A. Hickinbotham, *J. Chem. Soc. FARADAY Trans.* **1992**, 88, 2021.
[15]   W. G. Worley, *Dissolution kinetics and mechanisms in quartz- and grainite-water systems*, Ph. D. thesis, Massachusetts Institute of Technology, **1994**.
[16]   R. Li, H. Cheng, Y. Su, S. –W. Hwang, L. Yin, H. Tao, M. A. Brenckle, D. –H. Kim, F. G. Omenetto, J. A. Rogers, Y. Huang, *Adv. Funct. Mater.* **2013**, 23, 3106.
[17]   R. S. Lillard , G. S. Kanner , D. P. Butt , *J. Electrochem. Soc.* **1998** ,*145* , 2718
[18]   H. Hixson , P. M. A. Sherwood , *J. Chem Soc.* **1995**, *91*, 3593.
[19]   M. Petrova , M. Bojinov , S. Zanna , P. Marcus , *Electrochim. Acta* **2011**, *56*, 7899.

List of Symbols, Abbreviations, and Acronyms

ACRONYM	DESCRIPTION
AFM	atomic force microscopy
ALD	atomic layer deposition
BOE	buffered oxide etchant
CMOS	complementary metal–oxide–semiconductor
CVD	chemical vapor deposition
DI	deionized
E-beam	electron beam
Fe	iron
FTIR	Fourier-transform infrared spectroscopy
HF	high frequency
HF	hydrofluoric acid
LF	low frequency
LPCVD	low-pressure chemical vapor deposition
Mo	Molybdenum
MOSFET	metal–oxide–semiconductor field-effect transistor
NM	nanomembrane
OLED	organic light-emitting diode
PBS	phosphate buffer solution
PCL	polycaprolactone
PDMS	poly(dimethylsiloxane)
PECVD	plasma-enhanced chemical vapor deposition
PGA	polyglycolic acid
PLA	polylactic acid
PLGA	polylactic-co-glycolic acid
RF	radio frequency
RIE	reactive ion etching
RT	room temperature
SEM	scanning electron microscope
SF_6	sulfur hexafluoride
SiO_2	silicon oxides

ACRONYM	DESCRIPTION
SOG	spin-on glass
SOI	silicon-on-insulator
TEM	transmission electron microscopy
W	tungsten
XPS	x-ray photoelectron spectroscopy
XRD	x-ray diffraction
XRR	x-ray reflectometry
Zn	zinc